

UNIVERSITY OF OKLAHOMA

GRADUATE COLLEGE

ADDITIVE MANUFACTURING OF HDPE USING SELECTIVE LASER  
SINTERING

A THESIS

SUBMITTED TO THE GRADUATE FACULTY

In partial fulfillment of the requirements for

Degree of

MASTER OF SCIENCE

By

BENJAMIN HOELZEL  
Norman, Oklahoma  
2019

ADDITIVE MANUFACTURING OF HDPE USING SELECTIVE LASER  
SINTERING

A THESIS APPROVED FOR THE SCHOOL OF AEROSPACE AND MECHANICAL  
ENGINEERING

BY

Dr. Yingtao Liu, Chair

Dr. Mrinal C. Saha, Co-Chair

Dr. Jivtesh Garg



## **Acknowledgements**

I would first like to thank Professor Yingtao Liu at the University of Oklahoma (OU) for providing me the opportunity to further my education in the field of engineering with his research group. I am thankful for the privilege of being a founding member of his additive manufacturing research team that is on the brink of many great accomplishments. I am also extremely grateful for the constant guidance, mentorship, encouragement, friendship, and push to better myself that he provided throughout my two years of working with him. In addition, I would like to thank Professor Mrinal Saha for his wisdom and guidance each week during our meetings as well as being a constant resource for my research and graduate studies during my two years working with him. I would also like to thank Professor Jivtesh Garg for taking the time in and out of the classroom to aid in my graduate studies as well as taking interest in my research as a member of my thesis committee.

The past two years of research and school have been very enjoyable largely because of the people I have met and had the privilege of working with. I am very thankful for my friends Mohammad Charara, Blake Herren, Noah Golly, Weston Sleeper, Colin Bray, Ryan Cowdrey, and Emmanuel De Leon with whom I have had the pleasure of seeing and working with every day. Our research team has been a blessing as it was filled with hard work, dedication, teamwork, support, enjoyment, encouragement, and mutual respect that I will cherish and take with me in all my future team settings. I want to also thank my friends Coltan Bliss, Aaron Craig, Antonio Santiago, Joe Paul Crawl, Matt Police, Kovi Barlow, Dillon Baker, and Zack Martin for taking the time to help me with various tasks that made my research possible. Along with them, I want to thank the fantastic AME staff

at OU including Bethany Burklund, Martina Ferguson, Melissa Foster, Ellen McKenzie, Rebeka Morales, Billy Mays, and Greg Williams. Without their guidance, support, and advice I would not have been able to accomplish my goals.

Finally, I want to thank my closest friends and family. I would first like to thank my roommates David Lagunes, Jack Palmer, Logan Lambert, and Chance Nevarez for their constant support even during the most stressful of times. Along with my roommates, my family has been there during the roughest of times and I am grateful for the love, support, and sacrifice my parents, Shawn and Karen Hoelzel, as well as my brother and sister Blake and Aubin Hoelzel have given me.

## **Dedication**

I want to dedicate this thesis to my family Shawn, Karen, Blake, and Aubin Hoelzel who have given endless love and support and have taught me to follow my dreams. I would also like to dedicate this thesis to my Grandpa John Hoelzel Sr. who got me interested in engineering at a young age by providing his own wisdom and experiences as a professional engineer.

## Table of Contents

Acknowledgements.....	iv
Dedication.....	vi
Table of Figures.....	ix
Table of Tables.....	xii
Abstract.....	xiii
CHAPTER 1: INTRODUCTION.....	1
Section 1.1: State of the art of 3D printing for polymers.....	1
Section 1.2: Fused Deposition Modeling (FDM).....	3
Section 1.3: Stereolithography (SLA).....	5
Section 1.4: Material Jetting.....	7
Section 1.5: Selective Laser Sintering (SLS).....	8
Section 1.6: Comparison of Techniques.....	10
Section 1.7: Thesis Outline.....	12
Chapter 2: Design and Optimization of SLS printer.....	14
Section 2.1: Introduction.....	14
Section 2.2: Mechanical Design.....	15
Section 2.3: Electrical Components.....	22
Section 2.4: Optimization of the JRLS.....	29
Chapter 3: 3D Printing of HDPE Samples.....	31

Section 3.1: Sample Modeling and G-Code Generation.....	31
Section 3.2: Printing Parameters.....	35
Section 3.3: Single Layer Samples .....	37
Section 3.4: Multi-Layer Samples .....	38
Section 3.5: Printed Complex Geometries.....	43
Section 3.6: Measurement and Geometry Shape Validation .....	46
Chapter 4: Mechanical Testing of the 3D Printed Samples .....	50
Section 4.1: Density Tests.....	50
Section 4.2: Scanning Electron Microscope Tests.....	52
Section 4.3: Tensile Tests Results of SLS Printed Samples .....	58
Section 4.4: Printed Sample Tensile Test Results Compared with Casted Samples ..	67
Chapter 5: Conclusions and Future Work.....	76
References.....	79



## Table of Figures

Figure 1: FDM Process [9] .....	4
Figure 2: SLA Process [10].....	6
Figure 3: Material Jetting Process [9].....	7
Figure 4: SLS Process.....	9
Figure 5: Completed JRLS 1000.....	15
Figure 6: The Wooden Piston Block [1].....	16
Figure 7: Aluminum Frame [1].....	16
Figure 8: The Build Plate Piston.....	17
Figure 9: Build and Feed Plate Movement and Control .....	18
Figure 10: Front Side of the Sweeper .....	19
Figure 11: Back Side of the Sweeper.....	19
Figure 12: The Heat Chamber.....	20
Figure 13: X and Y Dimensional Laser Control.....	21
Figure 14: X Movement of the Laser.....	21
Figure 15: Y Movement of the Laser.....	22
Figure 16: 2560 Arduino Mega Board and Ramps 1.4 Board .....	23
Figure 17: LCD Screen .....	24
Figure 18: Heated Build Plate.....	24
Figure 19: Heat Bed Validation .....	25
Figure 20: Laser Source and Voltage Regulator.....	26
Figure 21: SSR and Ceramic Heaters .....	27
Figure 22: The MLX90614ESF IR-Thermometer .....	28

Figure 23: Ramps Board Schematic [1].....	28
Figure 24: Bed Leveling Spring and Wing-bolts.....	30
Figure 25: Simple Rectangular Prism Design and Dimensions.....	32
Figure 26: ASTM D638 Type V Dogbone Design and Dimensions.....	33
Figure 27: Rectangular Prism Sample G-code in Repetier Host.....	34
Figure 28: ASTM D638 Type V Dogbone G-code in Repetier Host.....	34
Figure 29: Cylinder Print First Layer.....	38
Figure 30: D638 Type V Dogbone First Layer.....	38
Figure 31: The Sintering Window [2].....	39
Figure 32: D638 Type V Dogbone Curling During Printing.....	40
Figure 33: Number of Print Layers vs. Print Type.....	41
Figure 34: Multi-Layer D638 Type V Dogbone Sample.....	42
Figure 35: Printed Cylinder.....	43
Figure 36: Cylinder Measurement Locations.....	44
Figure 37: Average Diameter at each Height Location.....	44
Figure 38: Average Diameter at each Diameter Location.....	45
Figure 39: Hollow Tube with Larger Base.....	46
Figure 40: ATSM Standard D638 Type V Dogbone Dimensions.....	47
Figure 41: Dogbone Geometry Measurement.....	47
Figure 42: Average Thickness vs. Print Type.....	48
Figure 43: Average Density with Respect to Printing Type.....	51
Figure 44: Print Type I.....	52
Figure 45: Print Type II.....	53

Figure 46: Print Type III.....	54
Figure 47: Print Type IV.....	55
Figure 48: Energy Density for each Print Type.....	56
Figure 49: Percentage of Voids.....	58
Figure 50: Standard D638 Type V Dogbone dimensions [22].....	59
Figure 51: Instron Tensile Testing Setup.....	60
Figure 52: Type I Print Stress Strain Curve.....	62
Figure 53: Print Type II Stress Strain Curve.....	63
Figure 54: Print Type III Stress Strain Curve.....	64
Figure 55: Print IV Stress Strain Curve.....	65
Figure 56: Casted Sample Mold.....	68
Figure 57: Printed vs. Casted Average Density.....	69
Figure 58: Printed vs. Casted Average Thickness.....	70
Figure 59: Printed vs. Casted Average Maximum Stress.....	71
Figure 60: Printed vs. Casted Average Maximum Stress.....	72
Figure 61: Printed vs. Casted Average Maximum Stress.....	73

## Table of Tables

Table 1: Categorization of Additive Manufacturing.....	2
Table 2: Summarization of Popular 3D Printing Techniques of Polymers [4].....	11
Table 3: Non-Changing Print Parameters.....	35
Table 4: Variable Print Parameters.....	36
Table 5: Average Print Layers for Each Print Type.....	41
Table 6: D638 ASTM Dogbone Dimensions Compared to Printed Dimensions.....	48
Table 7: Thickness Geometry.....	49
Table 8: Print Type Average Density.....	51
Table 9: Energy Density from Parameters.....	57
Table 10: Percentage of Voids.....	58
Table 11: Comparison of Maximum Stress, Strain, and Modulus.....	65
Table 12: Average Density and Thickness of Each Print Type.....	67
Table 13: Printed vs. Casted Density and Thickness.....	71
Table 14: Printed vs. Casted Stress, Strain, and Modulus.....	74

## **Abstract**

Selective Laser Sintering (SLS) is an additive manufacturing technique that bonds solid powder particles into complex 3-Dimensional (3D) shapes. These objects are constructed by repeatedly sintering or fusing layers of powder onto a build plate until the completed part is developed. Through the aid of an open source computer software known as Repetier Host, the desired component is sliced into many cross-sectional layers that are pathed out by a laser. Each new layer is created by new powder being deposited onto the previous layers and again a laser tracing out the cross-sectional path defined by Repetier Host. This technique has become more popular of recent as SLS allows for superior mechanical properties of printed components as well as the lack of required support material due to the excess powder around the print. On the other hand, High Density Polyethylene (HDPE) is a type of thermoplastic that has a high strength to density ratio and can be developed into complex components using SLS. As such, this thesis investigates and reports on the production and characterization of HDPE samples using SLS. The SLS machine used in this thesis was modified from an online design to allow both an affordable way to run experiments with HDPE powder and to truly understand the parameters and specifications needed to print HDPE powder into complex geometries. After running various test prints with HDPE, it was concluded that the most influential factors of successfully printing HDPE involve the ambient chamber temperature around the print, the temperature of the build plate, the laser intensity, the laser scanning speed, and the thickness of each layer. These five factors are crucial for keeping the temperature of the entire sample uniform and inside the sintering window, eliminating the natural tendency of HDPE samples to warp and deform during the printing process. Results show that these

influences also directly impact the geometry accuracy, density, and mechanical properties of the printed samples. Finally, the characterization results from the printed HDPE samples were compared to characterization results of casted samples at similar densities and geometries.

## **CHAPTER 1: INTRODUCTION**

### **Section 1.1: State of the art of 3D printing for polymers**

Three-dimensional (3D) printing, a subset of additive manufacturing (AM), is defined by the American Society of Testing and Materials (ASTM) as “*a process of joining materials to make objects from 3D model data, usually layer upon layer, as opposed to subtractive manufacturing methodologies*” [3]. AM is a field full of evolving technologies that fabricate metals, polymers, ceramics, and composites [4]. Out of these materials, polymers are currently the leader in progressing multifunctional and multipurpose 3D printing due to the wide variety of mechanical properties polymers possess. Specific polymers that can be 3D printed consist of thermoplastics, thermosets, elastomers, hydrogels, polymer blends, and polymer-based composites [4]. While most AM techniques in commercial industries focus on manufacturing metal components, 3D printing was first developed in 1986 by Charles Hull, who fabricated highly complex parts out of liquid resin polymers through his patent an “apparatus for production of three-dimensional objects by stereolithography” (US patent 4575330) [5]. Stereolithography is a vat photopolymerization 3D printing technique that will be further discussed in Section 1.3. Since the 1980s, the 3D printing industry has blossomed into a multibillion dollar industry as it continuously grows each year and was worth over \$6 billion in 2016 [6]. Due to this rapid growth, advances have been made for Charles Hull’s original technique of 3D printing polymers using stereolithography as well as new developments of other 3D printing techniques for rapid prototyping polymers. Table 1.1 below illustrates the entire spectrum of AM techniques available along with the material used with each technique.

**Table 1: Categorization of Additive Manufacturing**

<b>AM Category</b>	<b>AM Technology</b>	<b>Materials</b>
Binder Jetting	Ink-jetting S-print M-print	Metal Polymer Ceramic
Directed Energy Deposition	Direct Metal Deposition Laser Deposition Laser Consolidation Electron Beam Direct Melting	Metal Powder Metal Wire
Material Extrusion	Fused deposition modeling Fused filament fabrication 3D Bioprinting	Polymer
Material Jetting	Inkjet printing	Photopolymer Wax
Powder Bed Fusion	Selective Laser Sintering Selective Laser Melting Electron Beam Melting	Metal Polymer Ceramic
Sheet Lamination	Laminated Object Manufacturing Ultrasonic Additive Manufacturing	Hybrids Metallic Ceramic
Vat Photopolymerization	Stereolithography Digital Light Processing Two-Photon Polymerization	Photopolymer Ceramic

Out of these categories, the main processes used for 3D printing polymers are material extrusion, material jetting, powder bed fusion, and vat photopolymerization [4]. Within these main categories, the major techniques for 3D printing polymers that this chapter will define and discuss are fused deposition modeling which falls under the material extrusion category, stereolithography which is part of the vat photopolymerization category, basic material jetting which is its own category, and selective laser sintering under the powder bed fusion category. These four techniques were chosen to be discussed due to their popularity and relevance for printing polymer samples for engineering and scientific applications. Selective laser sintering is the 3D printing technique used in this thesis to print high density polyethylene (HDPE) samples, a type of thermoplastic, for mechanical testing that is further discussed in Chapter 4.



## **Section 1.2: Fused Deposition Modeling (FDM)**

Fused deposition modeling (FDM) was developed in 1988 by Scott Crump, the founder of Stratasys, Inc., and it involves the extrusion and deposition of a molten filament of polymeric material onto a substrate [7]. The ASTM defines fused deposition modeling as “*a material extrusion process used to make thermoplastic parts through heated extrusion and deposition of materials layer by layer; term denotes machines built by Stratasys, Inc*” [3]. The FDM process can be compared to the simple example of a hot glue gun extruding melted glue on to a surface. Filament, usually on a spool, is fed through a thin tube leading to a heated liquefier, which melts the solid filament into molten liquid filament. The solid filament entering the heated liquefier acts like a piston pushing the melted filament through a print nozzle of reduced diameter and solidifies upon leaving the nozzle [8]. All of this takes place on a gantry that is controlled with stepper motors in two directions, allowing the molten filament to be extruded onto the build surface that is also controlled by stepper motors in one direction ultimately allowing for complex 3D objects to be created [9]. Most FDM printers use stepper motors to move the gantry freely in a horizontal x-y plane and the build plate in a vertical z-plane. However, it is worth noting that there are some FDM printers, such as the Creality Ender Series printers and the CR-10 Series printers, that control the gantry in a vertical x-z plane with the build plate moving in just the y-direction.

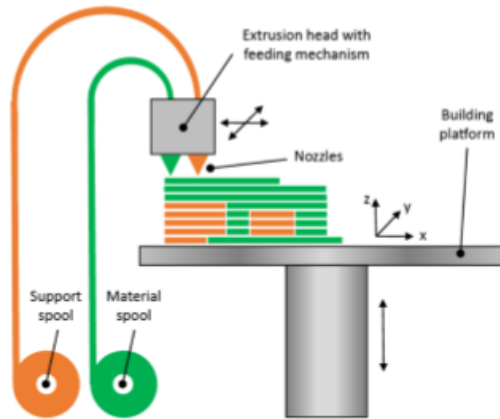


**Figure 1: FDM Process [10]**

Figure 1 illustrates the FDM process where the gantry moves horizontally in the x and y directions while the build plate moves vertically in the z-direction. This figure displays two nozzles on the gantry, one for the support material and one for the component material. Common FDM processes are the same as in Figure 1 except with only one nozzle depositing both the support material and the component material [11]. Support material is used for complex parts that cannot support themselves on their own during the printing process and can be easily removed once the print is completed. The most common materials used for FDM printing are polylactic acid (PLA) and acrylonitrile butadiene styrene (ABS) with standard filament diameter of 1.75 mm or 3 mm [10]. While there are several other materials that can be FDM printed, PLA and ABS are typically used as these are usually the only materials that commercial FDM printers are designed to print. FDM and similar extrusion processes are the most popular form of 3D printing polymers as they are the most commercially available to the public [12], [9]. FDM has advantages such as the ability to optimize prints for strong material properties and the overall low costs of the printers themselves. Disadvantages of this AM technique include the need for post processing due

to low resolution and poor surface finishing as well as high residual stresses in the printed components [13], [14].

### **Section 1.3: Stereolithography (SLA)**

This section focusses on the additive manufacturing technique known as stereolithography (SLA) which is defined by the ASTM as “*a vat photopolymerization process used to produce parts from photopolymer materials in a liquid state using one or more lasers to selectively cure to a predetermined thickness and harden the material into shape layer upon layer*” [3]. As briefly mentioned in Section 1.1, SLA was the first AM technique developed by Charles Hull in 1986 and uses a laser to cure liquid resin polymer layer by layer into complex 3D products [5]. Photosensitive liquid polymer filled in a vat or bath is required for the SLA process [5]. Typically for SLA, an ultraviolet (UV) light or laser source is controlled with stepper motors in the horizontal x and y-directions and a build plate platform, also controlled with stepper motors, is moveable in the vertical z-direction. With the build plate located just under the surface of the resin, usually the thickness of each layer, the UV laser traces the first cross-section of the desired print [15]. Once the trace is completed, the build plate is lowered the thickness of each layer and a sweeper applies a new layer of resin on top of the previously cured layer. The UV laser then traces the next layer and the process continues until the entire print is completed [5]. It is worth mentioning that some SLA printers have the UV laser on the bottom of the printer shooting up into a clear glass vat filled with polymer with the build plate moving up in the vertical direction for each layer, which utilizes gravity to add new resin for each layer as the resin flows underneath the previously cured layer when the build plate is raised.

The significance of this SLA design is that there is no need to incorporate a sweeper as gravity covers each previously cured layer with new liquid polymer resin.

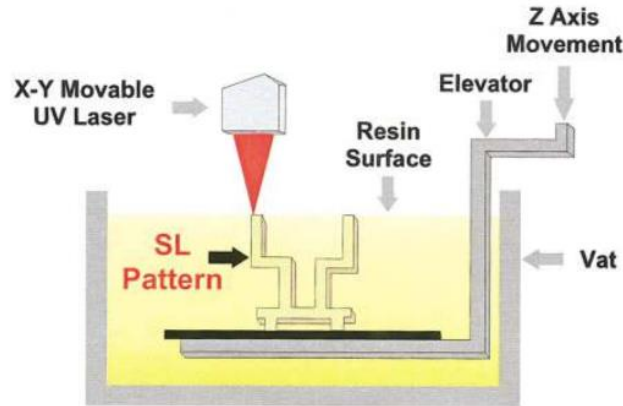


*Figure 2: SLA Process [16]*

Figure 2 shows the first type of SLA process discussed where the UV laser is controlled in the x and y-directions while the build plate is controlled in the vertical z-direction. This design, similar to the inverted SLA design discussed, does not use a sweeper as the vat is very large and new resin flows over the printed part as it is lowered by the elevator. The biggest concern with not using a sweeper for this type of design is that if the liquid resin is extremely viscous, almost like a gel, then the top layer being cured may not be a smooth surface resulting in an uneven print. Typical advantages of SLA printing include a high resolution to build time ratio, good component durability, and lastly the ability to produce multi-material parts [17], [18], [19]. The issues with SLA are that each print requires support material, parts cannot be created within a closed volume because of the liquid environment, residual stresses occur due to shrinkage, and lastly that it is an expensive process due to the requirement for a vat change after each print [20], [21].

## Section 1.4: Material Jetting

According to the ASTM, material jetting is “an additive manufacturing process in which droplets of build material are selectively deposited” [3]. Material jetting, first developed at the Massachusetts Institute of Technology (MIT) in 1995, creates 3D components out of jetted photopolymer droplets. These droplets are ejected onto a build plate as one or more print heads move across the build plate [10].

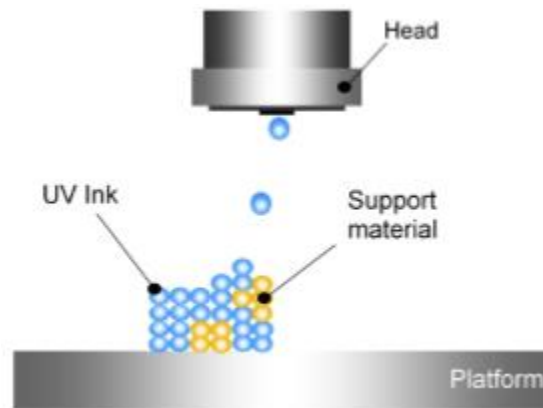


**Figure 3: Material Jetting Process [10]**

Figure 3 illustrates the two main components necessary for material jetting to work, a print head and build plate or platform. The layer change movement in material jetting is caused by either the print head raising after each layer or the build plate lowering after each layer. Typically for this AM technique, the print head can move in the x and y-axes while the build plate lowers. Most material jetting printers also use a UV curing source to cure the liquid polymer droplets once they have fallen to the build plate [4]. One material jetting printer that is similar to a normal inkjet paper printer is the material jetting printer patented by the company Objet. Instead of jetting ink droplets onto paper, this 3D printer jets layers of liquid photopolymer droplets onto a build plate that are cured with a UV light source

[5]. Iterations of these fine layers produce a 3D prototype that requires no post-curing [5]. A little bit of post processing is required for this AM technique as support material is again needed for complex parts that cannot support themselves. An advantage of material jetting is that two materials can be jetted at the same time to produce compound parts with different colors, patterns, textures, and mechanical properties [5]. Process variables such as print head speed, droplet velocity, and droplet frequency can be controlled to produce components with resolutions on the scale of 10-30  $\mu\text{m}$  [10]. Other advantages of this AM technique include low residual stresses and again high dimensional accuracy with the ability to print multiple materials [22], [23]. Some disadvantages are that the prints have weak mechanical properties due to the poor bonding between layers and there are adverse environmental effects on the produced prints [24], [25].

### **Section 1.5: Selective Laser Sintering (SLS)**

Selective laser sintering (SLS) is defined by the ASTM as *“a powder bed fusion process used to produce objects from powdered materials using one or more lasers to selectively fuse or melt the particles at the surface, layer by layer, in an enclosed chamber”* [3]. SLS bonds or sinters powdered materials into a solid object as the particles are heated by a laser to their glass transition temperature, the temperature just below their melting point. Most SLS printers partially melt the powders they are fusing, as the term “sintering” means to make a powdered material into a porous solid through the process of heating and applied pressure. The process of SLS printing begins with laying a thin first layer of powder onto the build plate. Then a laser, usually controlled in the horizontal x and y-directions by stepper motors, fuses the powder in the path of the cross-section of the desired component. Once the laser finishes the first layer, the build plate lowers the thickness of the next layer

in the vertical z-direction and the powder reservoir holding fresh powder raises the thickness of the next layer. A sweeper, controlled with stepper motors, then moves horizontally across the build plate carrying fresh powder from the powder reservoir onto the build plate covering the previously sintered layer. This process continues until the desired component is fully printed [26].

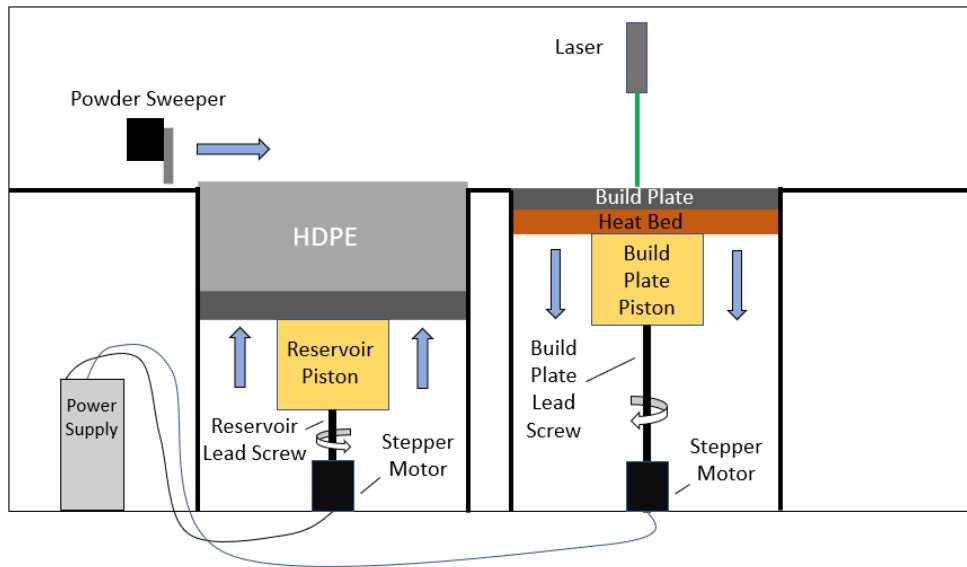


**Figure 4: SLS Process**

Figure 4 exhibits the described SLS process where a laser sinters the powdered material on the build plate that continuously lowers after each completed layer. This specific diagram uses lead screws and stepper motors to drop the build plate and raise the powder reservoir and uses stepper motors and timing belts to control both the laser and the sweeper. The main categories of polymers that can be sintered with SLS are Polyamide (PA), also known as nylon, Polyether ether ketone (PEEK), a type of thermoplastic with exceptional mechanical properties, Polystyrene (PS) based materials, and Polycaprolactone (PCL), a biodegradable polyester [5]. PA is by far the most versatile polymer for SLS as it comes in

different grades such as PA6, PA11, and PA12, where PA12 can also be carbon-filled and aluminum filled [5]. Typical particle sizes for SLS fall in the range of 10–150  $\mu\text{m}$  [27]. Advantages of SLS include superior mechanical properties of printed components as well as the lack of required support material due to the excess powder serving as the support making no post processing necessary [28], [29], [30]. The disadvantages of printing polymers with SLS are that there is high material waste, expensive costs for the materials used, only a few compatible materials available, and the presence of rough and grainy surface finishes caused by porous throughout and on the surfaces of the parts [31], [32].

Another application of SLS is the ability to manufacture complex metallic components. Metal laser sintering machines work like traditional SLS printers where thin layers of metal powder are sintered by a laser into the cross-section of the part and bonded layer by layer. As discussed, SLS sinters solid powder particles into a solid component. This phenomenon occurs because high temperature gradients cause no solid to liquid interface resulting in rapid solidification [33]. Rapid solidification, while beneficial for rapidly producing metallic parts, effects the microstructure features of the metal used because of higher cooling rates and dependent grain structures from the previous layers [34]. In turn, these microstructure affects directly influence the yield strength, elongation, ductility, and hardness of the material causing the mechanical properties to differ from traditional manufacturing processes [33]. Other issues include the density change, poor surface quality, presence of residual stresses, and need for support structures for heat dissipation and part orientation for smaller cross-sectional areas [33].

### **Section 1.6: Comparison of Techniques**

This section compares the four techniques that are typically used for 3D printing.



**Table 2: Summarization of Popular 3D Printing Techniques of Polymers [4]**

<b>Technique</b>	<b>Process</b>	<b>Advantages</b>	<b>Disadvantages</b>
Fused Deposition Modeling	<p>Step 1: Filament is heated and extruded through a nozzle in the path of the first layer</p> <p>Step 2: The build plate is lowered for the next layer</p> <p>Step 3: Steps 1 and 2 are repeated</p> <p>Step 4: Support Material is removed</p>	<ul style="list-style-type: none"> <li>▪ Can optimize prints for strong material properties</li> <li>▪ Cheap printer costs</li> </ul>	<ul style="list-style-type: none"> <li>▪ Post Processing due to support material</li> <li>▪ Low print resolution</li> <li>▪ Poor surface finishing</li> </ul>
Stereolithography	<p>Step 1: UV Laser cures first layer of liquid resin inside the vat in the path of the first layer</p> <p>Step 2: The build plate is risen the layer thickness</p> <p>Step 3: Steps 1 and 2 are repeated</p> <p>Step 4: Post curing and support material is removed</p>	<ul style="list-style-type: none"> <li>▪ High resolution to build time ratio</li> <li>▪ Quality component durability</li> <li>▪ Multi-material parts</li> </ul>	<ul style="list-style-type: none"> <li>▪ Post Processing due to support material and potential need for post curing</li> <li>▪ Limited to vat volume</li> <li>▪ Expensive Process</li> </ul>
Material Jetting	<p>Step 1: Liquid droplets are jetted onto the build plate and a UV light source may be used to cure the droplets</p> <p>Step 2: The build plate is lowered, or the print head is raised</p> <p>Step 3: Steps 1 and 2 are repeated</p> <p>Step 4: Support material is removed</p>	<ul style="list-style-type: none"> <li>▪ Multi-material prints</li> <li>▪ Low residual stresses</li> <li>▪ High dimensional accuracy</li> </ul>	<ul style="list-style-type: none"> <li>▪ Weak mechanical properties due to poor bonding between layers</li> <li>▪ Adverse environment effects</li> </ul>
Selective Laser Sintering	<p>Step 1: A laser source sinters the first layer of powder in the path of the first layer of the print</p> <p>Step 2: The build plate is lowered the thickness of the layer, the powder reservoir is raised the same distance</p> <p>Step 3: A sweeper covers the previous layer with new powder</p> <p>Step 4: Steps 1,2 and 3 are repeated</p>	<ul style="list-style-type: none"> <li>▪ Superior mechanical properties</li> <li>▪ No post processing</li> </ul>	<ul style="list-style-type: none"> <li>▪ High material waste</li> <li>▪ Expensive costs for the materials used</li> <li>▪ Few compatible materials available</li> <li>▪ Rough and grainy surface finishes</li> </ul>

The four techniques that are typically used for 3D printing polymers are summarized in Table 1.2 with the main process, advantages, and disadvantages given. As previously

mentioned, SLS is the 3D printing technique used for generating mechanical testing results of printed HDPE samples in this thesis. This technique was chosen due to the availability of powder HDPE for SLS printing as well as the desire to produce samples with excellent mechanical properties affordably. HDPE was used to also compare the printed properties to the properties of traditional casted samples because while available there is a lack of commercially developed HDPE parts with SLS [29]. Despite the expensive nature of this technique, the disadvantages of poor surface finishes are not of concern as this thesis is focused on the testing of the mechanical properties and measurement of porosity of the HDPE samples and not necessarily the print quality of the surfaces. Porosity is an important factor to measure when SLS printing due to the presence of tiny gaps in the powder particles that influence the material bonding. These gaps can be accounted for by using a finer UV laser, however, in general high porosity in SLS printed parts is bad as it produces poor bonding in the material and negatively influences the mechanical properties.

### **Section 1.7: Thesis Outline**

The purpose of this thesis is to affordably and successfully print HDPE using SLS and as a result is organized into five different chapters. In Chapter 2, the design and optimization of the SLS printer is presented including the mechanical design, the electrical components used, and the optimization of different features incorporated into the printer for print controllability. Chapter 3 displays the different 3D printed HDPE samples including one-layer samples, multiple layer samples, and complex shape samples. This chapter also includes the measurement and geometry shape validation of the printed samples. Chapter 4 provides the different mechanical testing of the 3D printed HDPE dogbone samples including density tests to determine the percentage of voids in the

samples, scanning electron microscope tests to determine the size of these voids, and tensile tests of the printed samples compared with casted HDPE samples. Finally, the conclusions and future work of this thesis are presented in Chapter 5.

## **Chapter 2: Design and Optimization of SLS printer**

### **Section 2.1: Introduction**

The selective laser sintering printer used for this thesis was constructed and modeled after the Johannes Rostek Laser Sintering 1000 (JRLS), a SLS printer developed by German engineer Johannes Rostek. The JRLS design was found on an open-source website called Instructables which enables people to post creative engineering projects with instruction guides inviting others to recreate their work. The JRLS Instructables guide included the basic design of the printer, the parts list, and a brief instruction guide on how the printer was developed [1]. The main reason this SLS printer was chosen to be modeled was because its design included a heat chamber which would allow the HDPE samples to be printed without the presence of curling or warping. Curling, which is further discussed in Section 3.4, occurs when there is a temperature gradient within the layers of the HDPE sample due to the print bed being hotter than the ambient temperature above the print bed. The heat chamber allows for the ambient temperature to be controlled and monitored in order to match the print bed temperature providing uniform temperature throughout the sample layers and eliminating curling off of the print bed.

Like the SLS printer in Figure 4, the JRLS utilizes two vertically controlled pistons to move the powder reservoir and build plate while controlling the laser in a horizontal x and y-plane above the build plate. A thin first layer of powder is deposited onto the print bed by the sweeper and then the laser sinters the material into the correct cross-section by completing the predefined path from the G-code. A thin first layer is important in order to properly get the part to adhere to the print bed. Once this layer is complete, the JRLS then lowers the print bed and simultaneously raises the feed chamber full of powder the

thickness of the next layer. Finally, the sweeper brings this new layer of powder over to the print bed and the laser then completes its next predefined path. This process continues until the complex component is fully printed like the process that was described in Section 1.5.

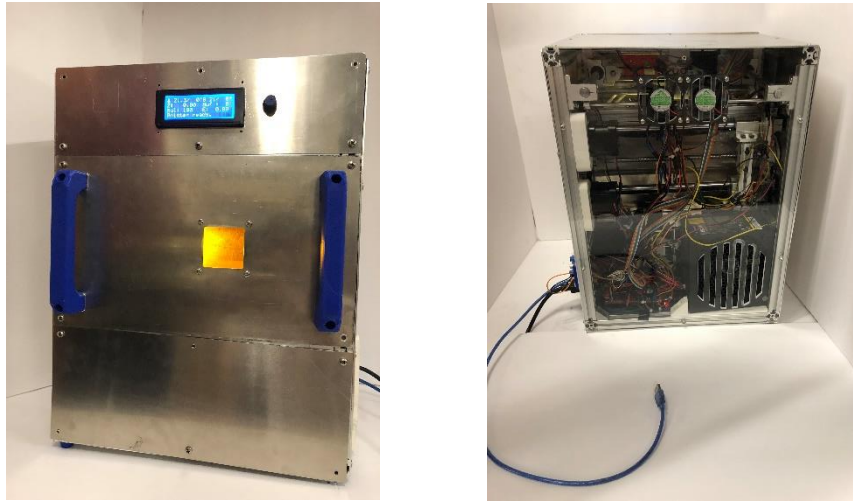


*Figure 5: Completed JRLS 1000*

Figure 5 above displays the JRLS 1000 that was built at the University of Oklahoma for the Additive Manufacturing Lab headed by Professor Yingtao Liu. The next section goes into detail about the main mechanical features implanted into the JRLS. These features include the wooden piston block, the mechanical frame, the feed and build plate pistons, the feed and build plate pistons' movement and control, the sweeper movement and control, the heat chamber design, and lastly the laser movement and control.

## **Section 2.2: Mechanical Design**

The JRLS was designed to be built from bottom to top where the first step involved constructing the wood piston block. The piston block, seen in Figure 6, is the wooden frame that supports both the print bed and the powder reservoir and separates the heat chamber

from the electronics. The piston block was created out of coated plywood for insulation and put together with metal screws. For even more insulation, the piston block was then coated again with aluminum tape to keep the electronics safe and the block itself from the presence of the extremely hot heat chamber.



*Figure 6: The Wooden Piston Block [1]*

Once the piston block was built, the aluminum frame was then constructed using the piston block as an internal backbone.

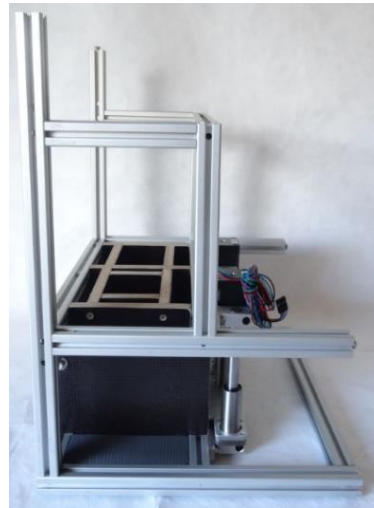


*Figure 7: Aluminum Frame [1]*

The frame was made from 2020, 1020, and 2040 aluminum extrusions. These aluminum extrusions were used because their slots allowed for M4 bolts and T-nuts to

bolt themselves to each other as well as allowed other attachments to be bolted such as the piston block shown in Figure 7. Developing the basic backbone of the printer allowed for the rest of the mechanical features to then be added.

Continuing with the bottom to top approach, the build plate piston and feed chamber piston were then implemented into the printer.

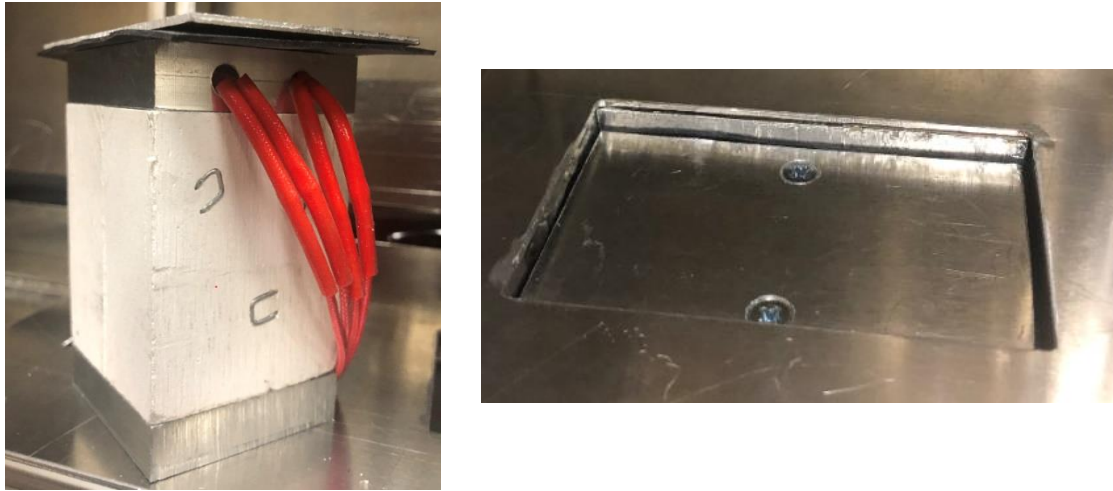


***Figure 8: The Build Plate Piston***

The pistons themselves can be seen in Figure 8 where both pistons are mechanically the same except that the build plate piston contains heating elements that will be further discussed in Section 2.2. Both pistons were built by sandwiching aluminum blocks to either side of a manufactured calcium silicate block. The top aluminum blocks serve as the points where the build plate and feed plate are mounted onto the piston and the bottom aluminum blocks serve as the points where the entire piston is mounted to the build and feed piston plates shown in Figure 9 below. Calcium silicate, an insulative material that can withstand over 900°C, was used to insulate and separate the top and bottoms of the build and feed pistons because the top portions of these pistons are subject to the heat of the heat chamber, as seen in Figure 8, and the bottom of these pistons are down by the electronics, as shown

in Figure 9 [1]. The dimensions of these pistons are roughly 3.5 inches tall with a 2 in x 2 in base area. The build plate was designed to be 85 mm x 55 mm and the feed plate was designed to be 90 mm x 55 mm.

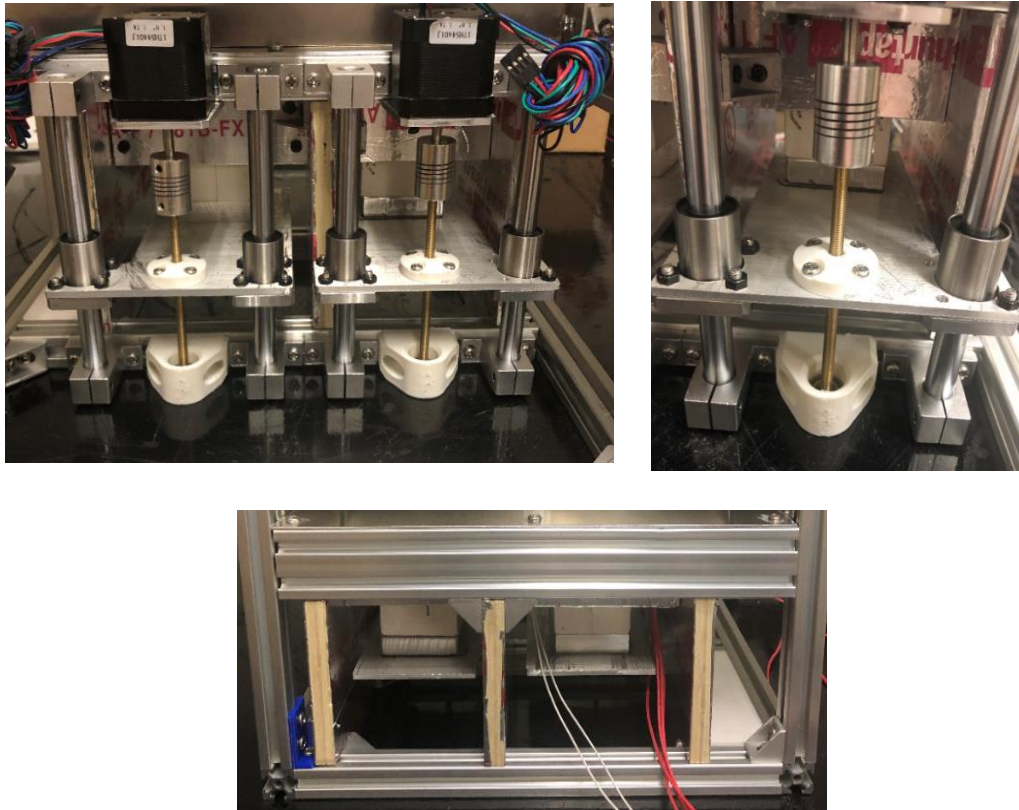


***Figure 9: Build and Feed Plate Movement and Control***

The vertical movement and control of the piston blocks are shown in Figure 9 through the aid of Nema 17 stepper motors and 8 mm threaded rods. Bolted to each piston plate is an ABS printed part holding a M8 nut in place allowing the plates to raise or lower depending on the direction the stepper motor rotates. As the stepper motors turn clockwise the pistons raise or climb up the threaded rods and when the stepper motors rotate counter-clockwise the pistons lower down the threaded rods. To support and guide the piston plates' vertical movement, bearings and smooth rods were placed on both sides of the pistons.



After the vertical build and feed plate movement was set in place, the horizontal sweeper movement and control was then developed. As previously mentioned, the purpose of the sweeper is to bring a new layer of powder from the feed chamber or powder reservoir to the print bed. Figure 10 illustrates the front side of the sweeper inside the heat chamber where this action occurs, and Figure 11 displays the back side of the printer where the sweeper is mechanically controlled.



*Figure 10: Front Side of the Sweeper*

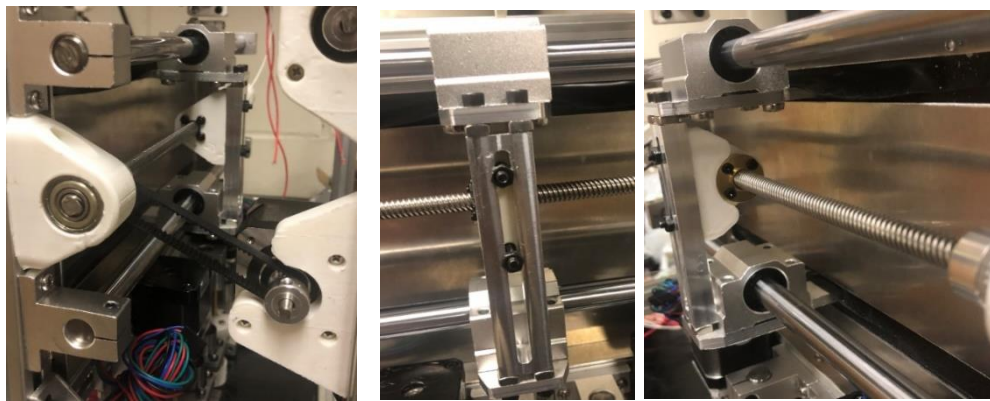


*Figure 11: Back Side of the Sweeper*

The front and back of the sweeper are divided by two sheets of aluminum with two slits cut. Sandwiched between these sheets is silicone rubber allowing for the front of the sweeper to be inside the heat chamber while also isolating the backside of the sweeper from the high temperature. Mechanically, the sweeper is controlled by a lead screw and nut. The nut is attached to the sweeper itself and as the lead screw is rotated, the sweeper moves in the X direction along the guided smooth rods. The lead screw is controlled and rotated by a stepper motor connected to a belt that is attached to a fixed pulley bore.

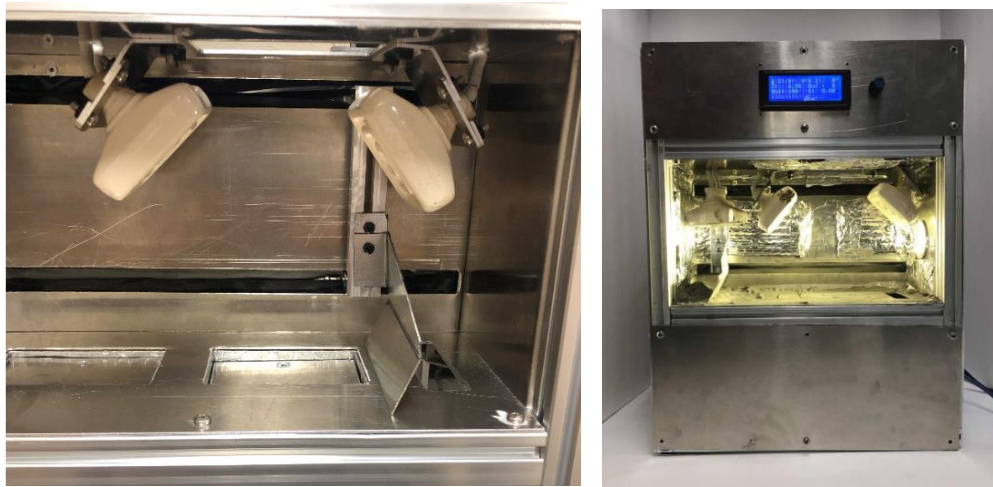


***Figure 12: The Heat Chamber***

The heat chamber, presented in Figure 12 above, is the most important part of the printer as it is the area where the sintering happens and was designed to withstand up to 150°C and HDPE samples could not be properly printed without a controllable heat chamber. The JRLS was designed to enclose both the print bed and feed chamber inside the heat chamber with aluminum walls. Aluminum was chosen as it can withstand the extreme temperatures and insulate the heat inside the chamber. The bottom of the chamber was designed to contain both the build and feed plates while the top of the heat chamber was manufactured with a rectangular hole the exact size of the print bed to allow for the laser to have full access of the bed. Attached to the top of the heat chamber are three 230V

ceramic heaters used to get the chamber to the desired temperatures. As mentioned with the sweeper, the backside of the heat chamber was designed to isolate the heat from the electronic components while also allowing the sweeper to move. The front of the heat chamber was designed to have a small window allowing the user to watch the print happen. Lastly, the side walls of the heat chamber were placed to enclose the heat chamber with the right side of the heat chamber containing a light fixated to light up the heat chamber to see the printing process.

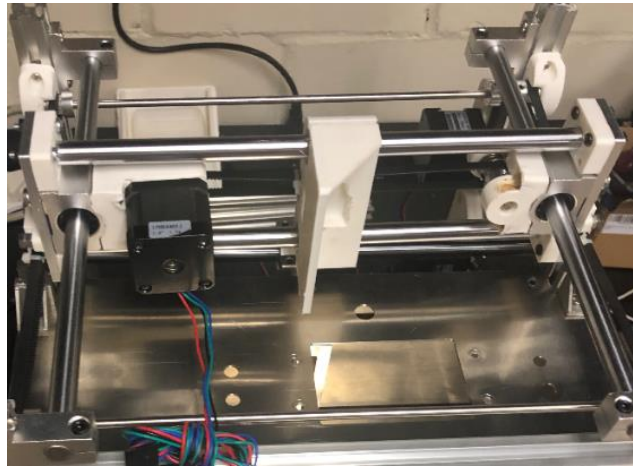


*Figure 13: X and Y Dimensional Laser Control*

The laser gantry is controlled in both the X and Y dimensions as it must be able to move anywhere above the print bed. Both dimensions are controlled with stepper motors and timing belts.



*Figure 14: X Movement of the Laser*

The X direction, which can be seen in Figure 14 above, is relatively simple as it only uses one stepper motor and one timing belt. The belt is fixed onto the laser gantry and as the stepper motor rotates, the laser is moved in either the positive or negative X direction along the fixed smooth rods. The Y direction, on the other hand, is controlled with one stepper motor and three timing belts and can be seen in Figure 15 below.



*Figure 15: Y Movement of the Laser*

The first belt is attached to both the stepper motor and a smooth rod that is oriented in the X direction. The smooth rod is connected to both the other belts that are then connected to the laser gantry on each side. As the stepper motor is rotated, the smooth rod turns and moves the timing belts attached to it. As a result, the laser gantry is controlled along the fixed smooth rods in either the positive or negative Y direction.

### **Section 2.3: Electrical Components**

Like the mechanical components discussed in Section 2.1, the JRLS printer possesses several key electrical features that allow it to operate. These electrical features consist of the 2560 Arduino Mega Board and Ramps 1.4 Board, the LCD screen, the heated build plate or print bed, the laser source and voltage regulator, the steady state relay (SSR) and ceramic heaters, and the MLX90614ESF IR-Thermometer.

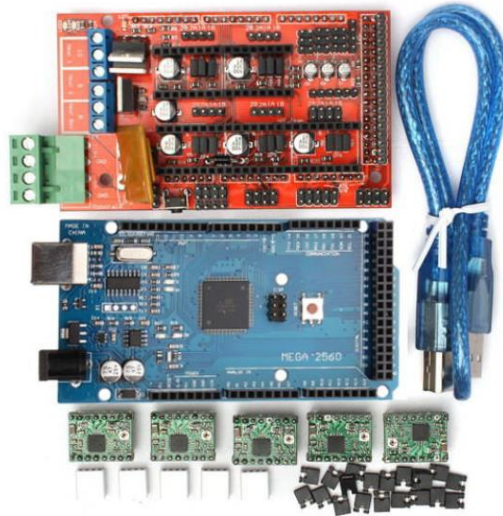


***Figure 16: 2560 Arduino Mega Board and Ramps 1.4 Board***

The Arduino Mega 2560 and Ramps 1.4 Boards are important features as they control all the electronics. The Arduino is a microcontroller that runs off an opensource platform and stores the printer's firmware. The firmware is the printer's main code that recognizes all the different components of the printer as well as each component's function. The Ramps board, which connects to the Arduino, is the board that controls each electrical component individually by sending the correct amount of voltage and current to the correct port during the printing processes. For example, when it is time to sweep a new powder layer in the printing process, the ramps board sends 12V to the port where the sweeper stepper motor is located for the duration of the completed sweeping process moving the sweeper the proper amount. These devices work together to recognize and execute the provided G-code which gives all the needed information to complete a print. The G-code for all the prints with the JRLS were created in an open-source slicer known as Repetier Host.

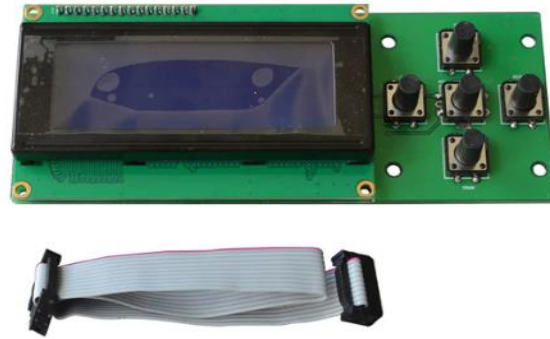


***Figure 17: LCD Screen***

The LCD screen, shown in Figure 17, connects to the ramps board and allows the user to control which G-code to run as well as monitor the bed temperature and chamber temperature. The LCD can also be used to preheat the printer and even test the different motors by moving them without running a print. The main significance of the LCD screen is that it is the extremal controller to run the JRLS.

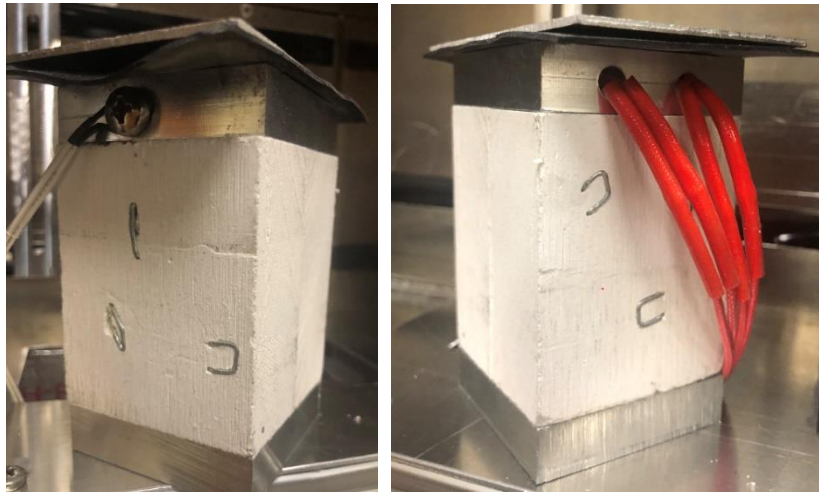


***Figure 18: Heated Build Plate***

Figure 18 displays the heated build plate, which was also discussed in Section 2.1, and is attached to the heated build plate piston where two 12V heaters and a thermistor are fastened into the top aluminum block on the piston. The two heaters are controlled and

regulated by the Ramps 1.4 board and the thermistor allows the temperature to be monitored on the external LCD screen. This is important because HDPE printing requires the heated bed to reach temperatures greater than 110°C. To validate the heat uniformity of the bed as well as ensure that heat bed readings from the thermistor were accurate, a Fluke Ti25 IR camera was used to capture the heat bed temperatures. Temperatures were tested both when setting the heat bed to 130°C with and without a layer of High Density Polyethene HP 260 (HP) tape ShurTech Brands, LLC covering the bed shown in Figure 19.

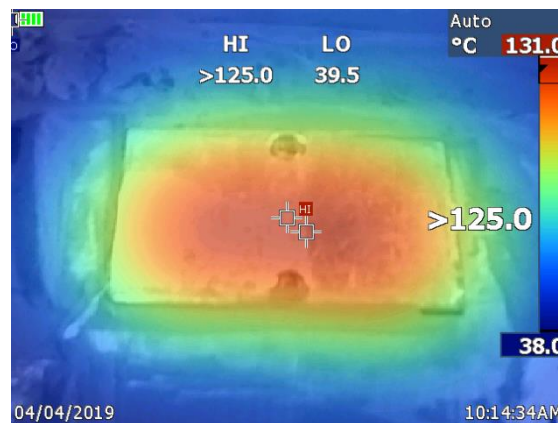


***Figure 19: Heat Bed Validation***

The image in Figure 19 is the IR Camera image of the heat bed set to 130°C without the HP tape layer. From this image it is shown that the heat bed thermistor while not perfect is still accurate with only a 1°C deviation. While not shown, the temperature of the bed with the HP tape only reaches 120°C even when set to 130°C. Therefore the bed temperature is off by 10°C due to the addition of the tape absorbing and blocking some of the heat. This difference is important as the prints were developed using the HP tape. However, the IR image shows that the middle of the bed is uniform while the edges have a significant temperature gradient present.

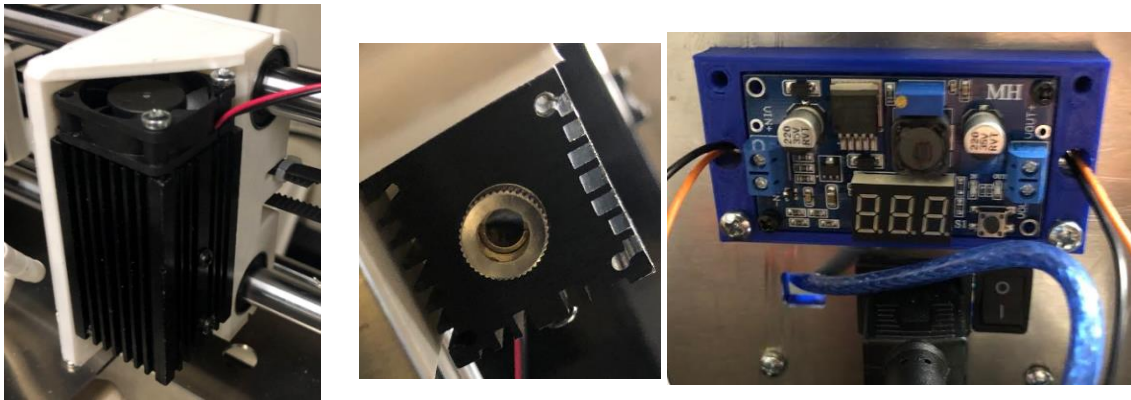


***Figure 20: Laser Source and Voltage Regulator***

The 1.8 W 445 nm laser with spot size 0.2 mm and its housing unit can be seen in Figure 20 above where the laser is secured inside a heat sink and mounted to the gantry. On top of the heatsink, a fan was attached to cool the laser during printing as small lasers when used for long durations such as a completed print have a problem with overheating. In order to control the laser intensity, the laser was connected to a voltage regulator, and while the ramps board gives the laser 12V, the voltage regulator was turned down to properly sinter and not melt the HDPE powder. Lastly, the focus of the laser is controlled by the laser cap and adjusted by turning.





***Figure 21: SSR and Ceramic Heaters***

The JRLS heat chamber is heated by three 230V ceramic heaters that can be seen in Figure 21. Because the power supply is only a 12V power source, the heaters are run with a steady state relay (SSR) which can also be seen in Figure 21. The SSR uses power from the main lines of the printer while also using the ramps board to complete the circuit. This means that the heaters are still controlled by the G-code and ramps because the heaters only turn on when the ramps give power to the correct pins and completes the circuit. The ability to control the heat chamber is extremely important because this is the only way to increase the ambient temperature around the HDPE samples and eliminate curling and warping.

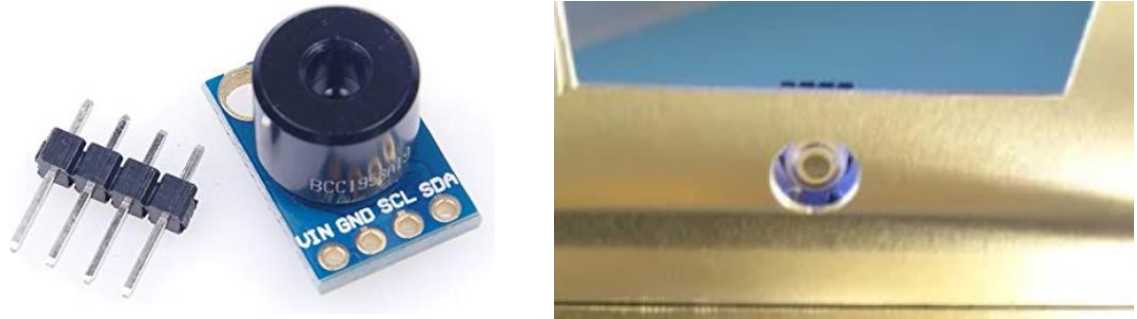


**Figure 22: The MLX90614ESF IR-Thermometer**

While the SSR powers the heaters, a MLX90614ESF IR Thermometer monitors them. This thermometer, which is displayed in Figure 22, is placed above the heat chamber and reads the temperature of the ambient temperature inside the chamber through a small hole cut into the ceiling of the chamber. The thermometer and ceramic heaters are PID controlled meaning that the thermometer gives feedback to the ramps board to control the heaters and maintain the desired ambient temperature set in the G-code and outputted on the LCD screen.

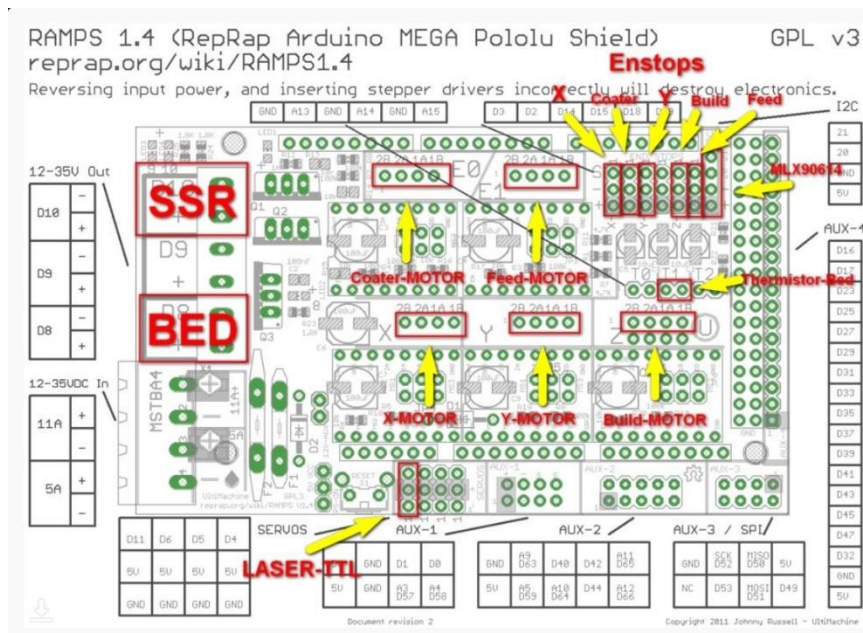


**Figure 23: Ramps Board Schematic [1]**

Lastly, Figure 23 displays how the ramps board is laid out with all the pins of where each electronic component connects to the board.

#### **Section 2.4: Optimization of the JRLS**

The University of Oklahoma's JRLS 1000 was closely modeled after the JRLS 1000 found on the Instructables website except with a few added modifications. Most of these modifications occurred in the heat chamber with the first being the addition of two extra ceramic heaters. The original JRLS only used one ceramic heater and to increase the time it took to heat the chamber, the new JRLS incorporated a total of three ceramic heaters. Along with the extra heater, an aluminum heat guide was placed inside the heat chamber and aluminum insulation tape was placed on the gaps of every wall. The heat guide was added to direct the heat down to the print bed to increase the ambient temperature closer to where the actual print occurs, and the aluminum insulation tape was used to sustain a high ambient temperature by keeping the heat from escaping the chamber. The last modification to the heat chamber was an addition of a glass plate to the ceiling of the heat chamber above the heat bed where previously there was a gap for the laser to project onto the bed. The addition of the secured glass plate not only allowed the laser to still project onto the heat bed but completely sealed the chamber allowing the ambient temperature to climb faster and stay hotter longer during printing.

Two new modifications on the print bed were also added to enhance the original JRLS. The original print bed size was only a 50 mm x 50 mm area but to print larger samples the print bed was increased to an 85 mm x 55 mm area. The second modification involved securing the build plate piston with springs and wing bolts to the piston plate allowing for the ability to level the bed with the tension in the springs shown in Figure 24.



***Figure 24: Bed Leveling Spring and Wing-bolts***

The original JRLS was unable to level the bed as the build plate was simply fixed to the piston plate. The overall controllability of this printer is what makes the JRLS unique.

HDPE is a difficult sample to print and having the ability to control the bed level, ambient temperature, bed temperature, and laser intensity makes printing HDPE possible.

## **Chapter 3: 3D Printing of HDPE Samples**

### **Section 3.1: Sample Modeling and G-Code Generation**

The G-code for the JRLS was generated through an opensource slicer software known as Repetier Host. Repetier Host allows for the user to upload custom printer and print settings to develop complex G-code capable for any type of 3D printing such as selective laser sintering. In tandem with the ability to create custom print and printer settings, Repetier Host also allows for complete control of the printer. This enables the ability to preheat the bed and heat chamber prior to printing. This also enables the user to manually control individual motors and test single lines of G-code to fine tune every detail of how the printer should operate during a print.

The first step in producing G-code involves modeling the desired sample using a Computer Aided Design (CAD) software. For this thesis, all CAD models were developed using SolidWorks 2018. The sample G-code that were modeled for this section included a rectangular prism model and an ASTM D638 Standard V dogbone model. These two samples were used in this section to show how both simple and irregular geometries were developed into G-code that was properly understood by the JRLS. Figures 25 and 26 below give the dimensions of the rectangular prism and ASTM D638 Type V dogbone.

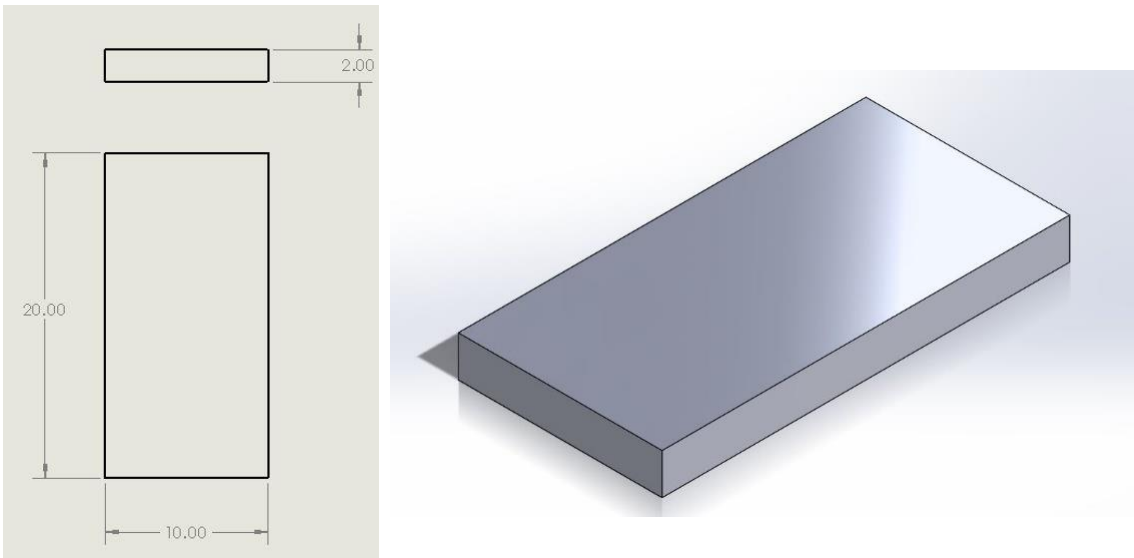


***Figure 25: Simple Rectangular Prism Design and Dimensions***

The dimensions of the simple rectangular prism shown above in Figure 25 were designed in millimeters and created for easy G-code creation with only a few layers. The ASTM D638 Type V dogbone design, however, was taken from the ASTM website further discussed in Section 4.3 and is shown below in Figure 26 with dimensions also presented in millimeters.

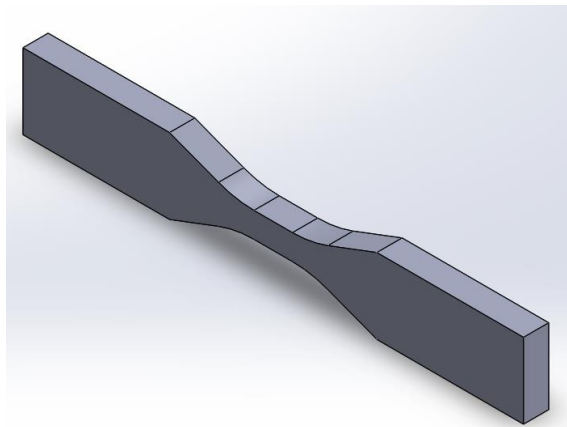
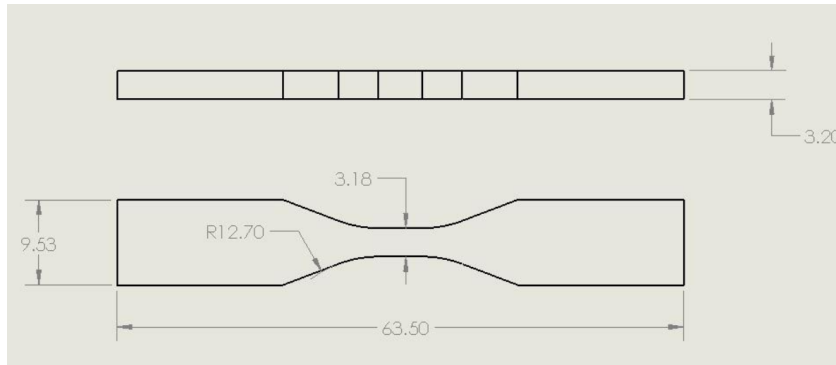


***Figure 26: ASTM D638 Type V Dogbone Design and Dimensions***

After modeling the samples in SolidWorks, the models were then uploaded into Repetier Host as STL file extensions. In Repetier Host, the G-code for each sample was generated using the custom settings set in the Repetier Host configuration. The main parameters that were used to generate each sample G-code and complete the finished prints are shown in Section 3.2 below. Using these settings, the modeled G-code for the rectangular prism sample is shown below in Figure 27 and the ASTM D638 Type V dogbone modeled G-code is shown in Figure 28 below.

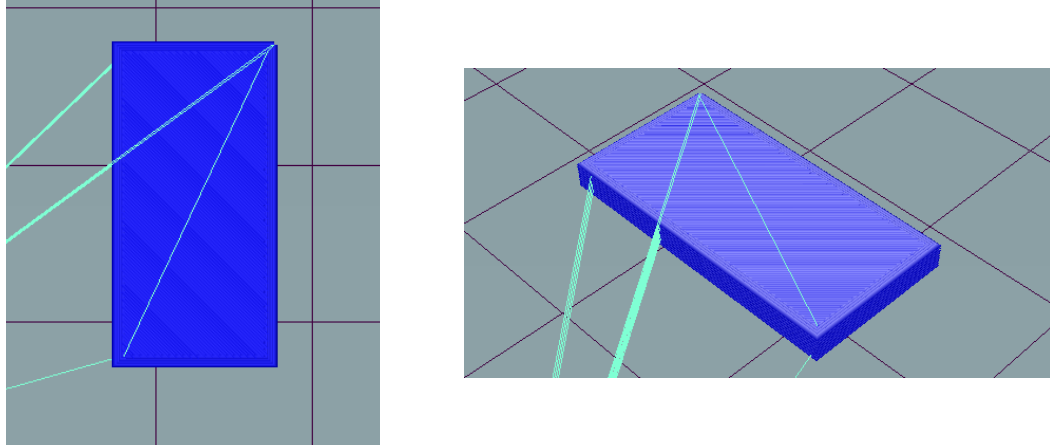


***Figure 27: Rectangular Prism Sample G-code in Repetier Host***

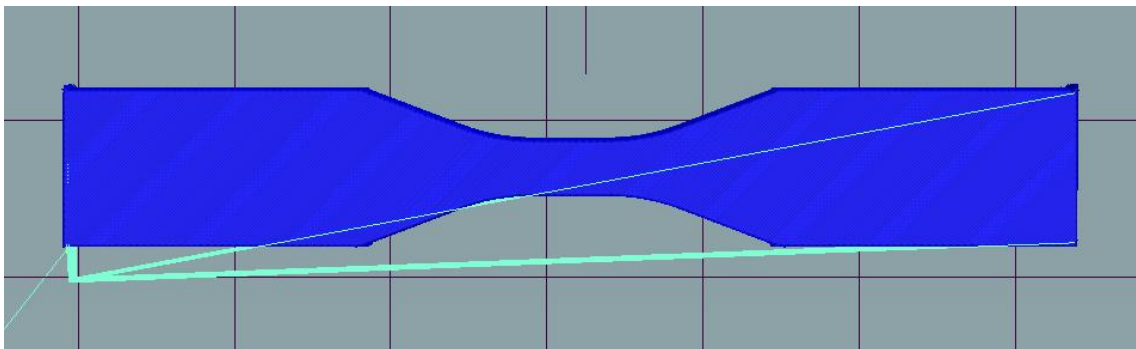
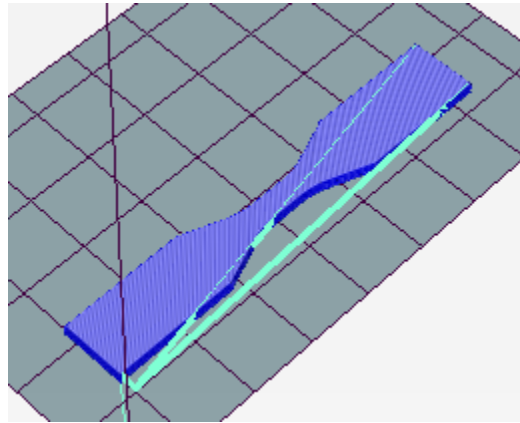


***Figure 28: ASTM D638 Type V Dogbone G-code in Repetier Host***

After developing the G-code, the final step to complete a print was uploading the G-code to the JRLS allowing it to access and print the desired geometry. While only the rectangular



prism and D638 Type V dogbone G-code are discussed in this section, all finished prints had to go through this process to be printed with the JRLS.

### Section 3.2: Printing Parameters

To successfully print HDPE with the JRLS, a variety of parameters were developed and fine-tuned. Overall there were four main printing parameter types developed but Table 3 below shows all the parameters that were held constant for each of the four main printing types.

**Table 3: Non-Changing Print Parameters**

Non-Changing Print Parameters	
Bed Adhesion	HP Tape
Bed Temperature	130°C
Layer Thickness	0.1 mm
Fill Density	100%
Fill Pattern	Rectilinear
Fill Angle	45°
Perimeters	None

The constant parameters shown in Table 3 were determined over time with a trial and error approach to see what worked best for the HDPE powder. Originally, the main issue with this powder involved it curling off the bed due to various reasons of poor bed adhesion as well as large temperature gradients. Because of this issue, HP tape was applied to the aluminum heat bed to allow the first layer to better adhere to the bed. The HP tape, which is also contains HDPE, was proven successful for first layer bonding as HDPE bonds well to itself. HP tape was not the only tape that was tested however it was the only tape that proved to aid HDPE bed adhesion. Typical bed adhesion temperatures for HDPE are around 115-120°C and setting the bed to 130°C resulted in the best bed adhesion for printed

components as the actual bed temperature only reached 120°C because of the partial heat blockage from the HP tape to the first layer [35]. After developing a properly bonded first layer, the next parameter that was tested was the layer thickness. Initially, large layer thicknesses of 0.3 mm and 0.4 mm were attempted as these are standard for 3D printing. These thicknesses, however, were too large and the laser was unable to properly sinter the top layer of powder to the previously sintered layers causing curling and delamination of prints. Moving smaller to 0.2 mm proved better however there were still issues with curling in the first few layers. Eventually, it was found that the best layer thickness was 0.1 mm which allowed the layers to properly bond together as well as not be ripped of the bed by the sweeper [36]. The fill density, fill pattern, and fill angle were also developed over time with trial prints and were eventually chosen due to the best presence of HDPE bonding and least amount of curling during the printing process. Lastly, the print perimeters were taken out of the G-code due to the thermal gradient development in the print edges from adding localized heat to the print either at the beginning or end of the print.

While the constant printing parameters were developed to fine tune the JRLS into consistently developing high quality samples, the next set of parameters including the chamber temperature, the printing speed, and lastly the laser intensity were tested to develop samples with the most optimal densities and mechanical properties [37].

***Table 4: Variable Print Parameters***

Print Type	Type I	Type II	Type III	Type IV
Chamber Temperature	110°C	120°C	120°C	120°C
Print Speed	10 mm/s	10 mm/s	10 mm/s	20 mm/s
Laser Power	3.8V	4.1V	4.2V	4.4V

Table 4 above displays the controllable parameters that had the most influence in the mechanical properties of the printed test samples that are further shown in Section 4.1. Using these different controllable parameters, four different types of printing parameter settings were developed causing different print properties and densities. The first variable parameter that was focused on was the ambient temperatures as this and the bed temperature are the main two settings that heat and sustain the print at a uniform temperature attempting to eliminate a temperature gradient from developing in the print. The next two controllable settings focused on were the laser power and laser speed. These two parameters are important for printing HDPE as they influence the localized heating that goes on during the sintering process.

### **Section 3.3: Single Layer Samples**

The first set of HDPE samples that were developed with the JRLS were single layer samples. The first layer of any SLS printed sample is the most important layer as it is where the printed sample adheres to the bed and is where the rest of the sample layers are bonded and secured to. As mentioned in Section 3.2 above, there were both fixed parameters and controllable parameters used for printing HDPE in this study. While the controllable parameters were mostly adjusted to test different mechanical properties of multi-layer prints, the fixed parameters were developed and fine-tuned specifically for the first and single-layer prints. Because of the early fine-tuning process, the first successful single layer prints were completed using printing Type I parameters and eventually single layer prints were completed with all four printing types as these first layers grew into multi-layer prints.



*Figure 29: Cylinder Print First Layer*



*Figure 30: D638 Type V Dogbone First Layer*

Figures 29 and 30 are the first layers of a cylinder and a D638 Type V dogbone. Both figures represent first layers using the Type IV printing type parameters shown in Table 4. Discussed further in Section 3.4, the Type IV printing parameters resulted in the largest number of print layers due to the least amount curling. Overall each of the settings provided in this chapter allow for first layers of any sample geometry to be successfully developed.

### **Section 3.4: Multi-Layer Samples**

The next set of HDPE samples that were developed with the JRLS included multiple layer samples. The difficulty in developing these samples was the battle with curling and warping of HDPE. Curling is the occurrence of shrinkage and warping of flat surface parts that result in curved profiles caused by uneven temperature gradients

throughout the sample layers [38]. To eliminate curling, all layers of the sample need to fall inside the sintering window.

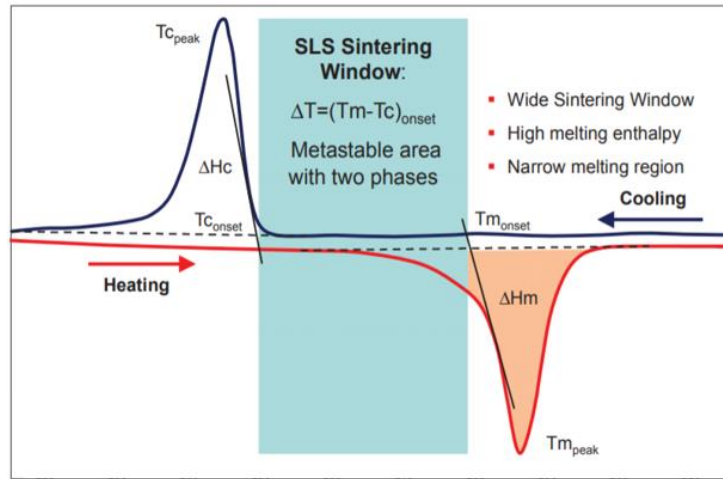


**Figure 31: The Sintering Window [2]**

The sintering window, shown in Figure 31, is located directly between the crystallization temperature and the melting temperature. Printing with less heat than the crystallization temperature will result in the powder not crystallizing or bonding together and printing with heat greater than the melting temperature will cause a thermal shock in the print resulting in curling and warping [2]. For HDPE this window falls between 116°C and 137°C [39]. Controlling the laser power and scanning speed of the laser are the keys to staying inside this sintering window. The laser power is what gives the powder energy to bond together and the scanning speed determines how much energy is given to the powder by controlling how long the laser is on a particular section of powder [40]. The energy density controlled by these two factors is calculated later using Equation 1.

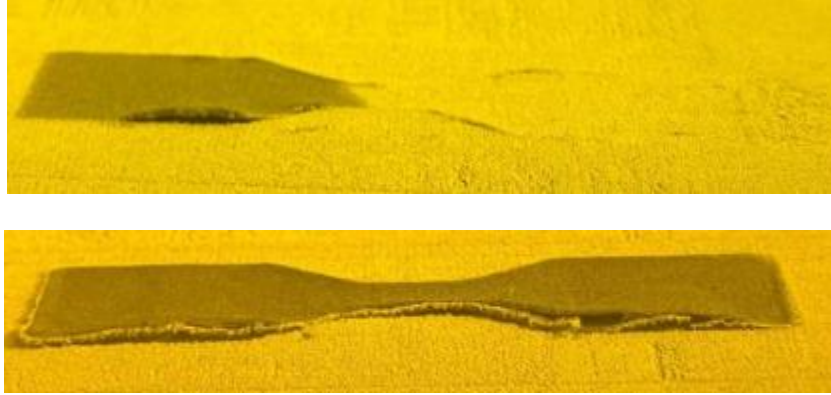


***Figure 32: D638 Type V Dogbone Curling During Printing***

The curling seen in Figure 32 shows both the initial signs of curling (top) as well as the later more devastating effects of delamination and curling off the bed (bottom). The main influences of curling are the three previously discussed variable printing parameters and one constant parameter of bed temperature, ambient temperature, laser power, and laser speed defined in Section 3.2. Print Type I mitigated curling in the first layer by testing the parameters shown in Table 3 until the entire single layer sample had a uniform temperature. Following the success of printing Type I, the other three printing types were developed specifically for multi-layer samples with each influencing the density, mechanical properties, and print layers of these multi-layer prints. The number of print layers of each printing type can be seen in Table 5 below and range from 5 to 11 layers with layer heights of 0.1 mm. For each print type, 3 samples were tested.

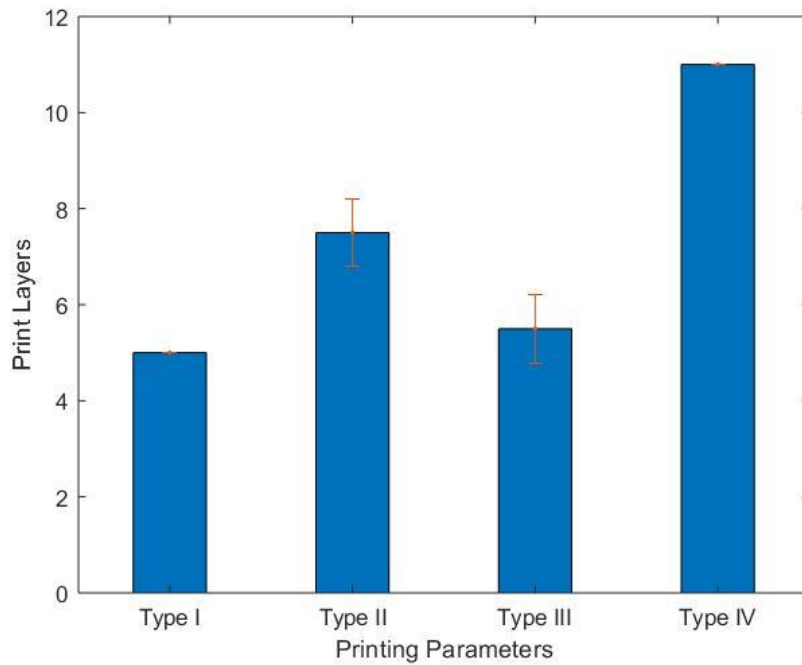


**Figure 33: Number of Print Layers vs. Print Type**

**Table 5: Average Print Layers for Each Print Type**

Print Type	Average Number of Print Layers
I	5.0 ± 0
II	7.5 ± 0.7071
III	5.5 ± 0.7071
IV	11.0 ± 0.7071

Both Figure 33 and Table 5 provide that, excluding Printing Type III, there is a positive trend that the increase in laser power also increases the number of layers that are printed. Increasing the number of print layers ultimately increases the overall print thickness which is important for larger components. The laser intensity plays a tremendous roll in increasing the print thickness because it controls the localized temperature of the powder. This is significant because to print larger and more complex components the prints must be free of thermal gradients which cause warping and curling. So, while Table 5 draws the

conclusion that the increase in laser intensity increases the number of print layers, which is true, it is better to understand that the laser intensity decreases the curling and warping in the printed components which in turn develops thicker components. Print Type III is an outlier to this assumption that the increase in laser intensity improves the number of layers that can be printed because Print Type III falls outside the sintering window better explained in Section 4.3. At a scanning speed of 10 mm/s, 4.2 V from the laser was too hot and therefore melted most of the sample layers resulting in a thermal shock in the HDPE that caused the print to curl earlier than print Type II. Print Type IV, while printing at an even greater laser intensity of 4.4 V, falls back inside the sintering window due to the increase in scanning speed from 10 mm/s to 20 mm/s and thus is able to print the greatest number of layers.

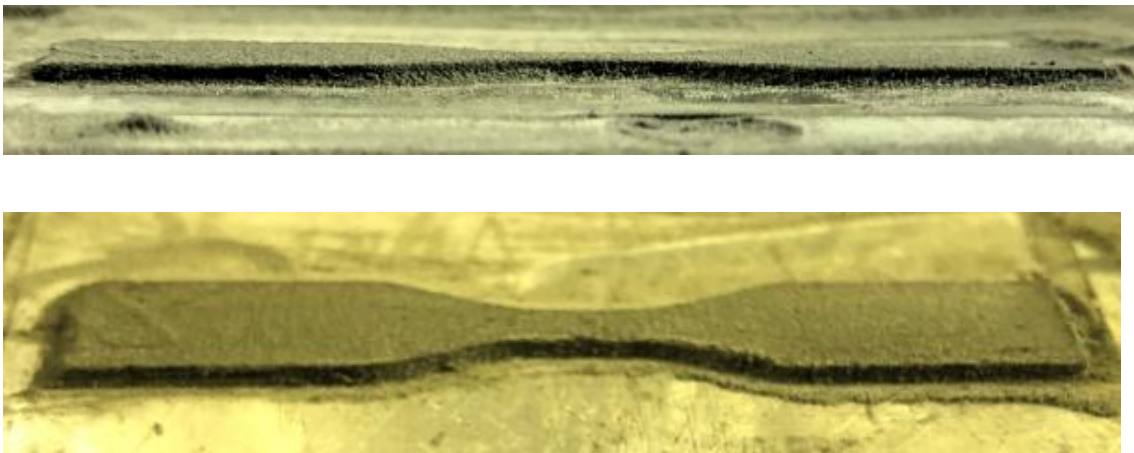


***Figure 34: Multi-Layer D638 Type V Dogbone Sample***

Figure 34 shows a successfully completed 15-layer dogbone sample without any curling. This sample is shown still adhered to the bed and was completed with Type IV parameters except with an increase of the laser scanning speed from 20 mm/s to 25 mm/s after 5 layers and then from 25 mm/s to 30 mm/s after 10 layers. This printing process of



increasing the speed as the print went on was stemmed by the success of printing with print Type IV. Increasing the scanning speed during the print kept the laser from overheating the later layers when not as much heat was needed to sinter the layer [41]. This new method that could be called print Type V is briefly mentioned again in Section 3.5 because of the improvements in larger and more complex components but is not further discussed in the tensile testing of the HDPE dogbones.

### **Section 3.5: Printed Complex Geometries**

The purpose of this section is to display the more complex prints developed with the JRLS to prove that it can produce components with more layers than the limited number of layers shown with the dogbones. Figure 35 below displays a printed 85-layer cylinder.

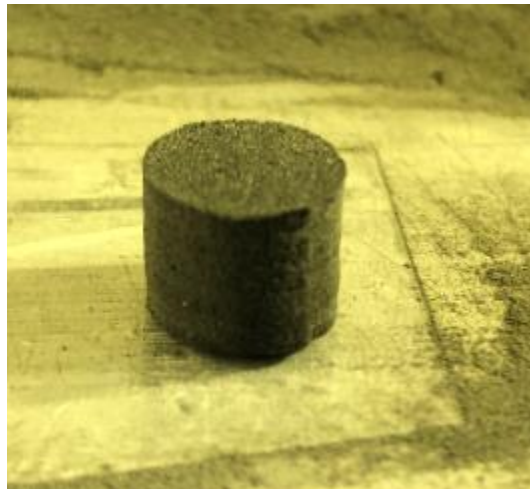


*Figure 35: Printed Cylinder*

The cylinder represented in Figure 35 had a 10 mm diameter with an 8.5 mm height. Using calipers, the diameters at four different locations were measured at three different heights shown in Figure 36 below.

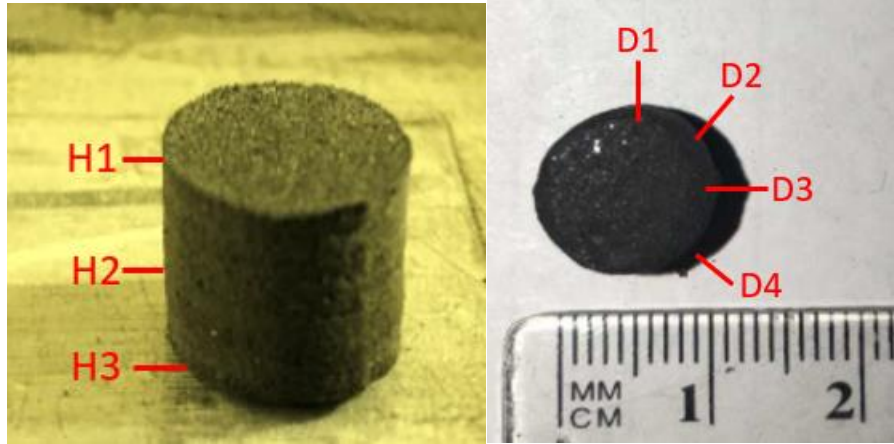


***Figure 36: Cylinder Measurement Locations***

From the measurements at these locations, the average diameter at each height and the average diameter at each diameter location were compared in Figures 37 and 38 below.

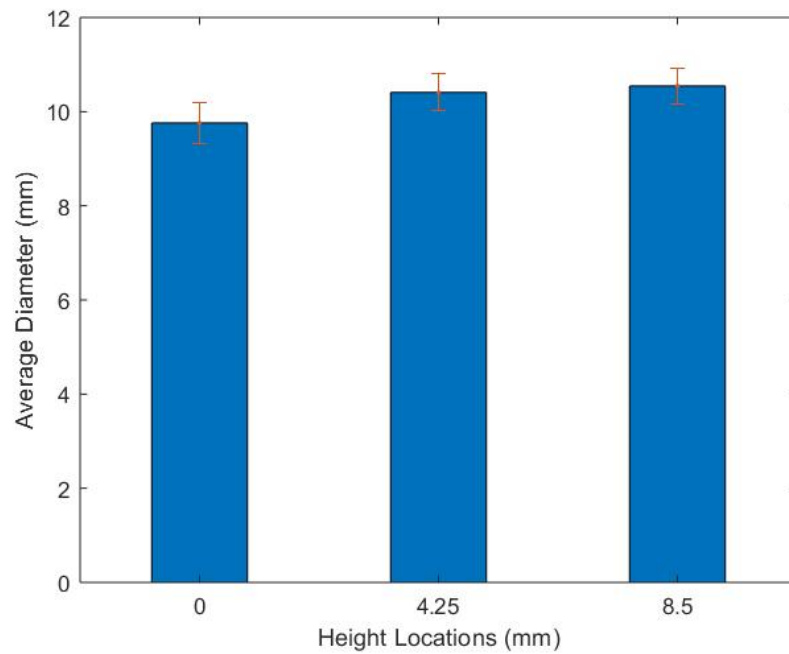


***Figure 37: Average Diameter at each Height Location***

Figure 37 above displays the change in diameter across the printed cylinder from bottom to top as the three height locations were taken at the top, middle, and bottom of the cylinder.

From the figure it can be seen that the diameter slightly increases. This is due to the print heating up during the printing process and slowly bonding excess particles around the desired cross-section with the excess heat absorbed and retained in the previously printed layers. This has been improved by slowly increasing the scanning speed after each layer during the later layers when this occurs.

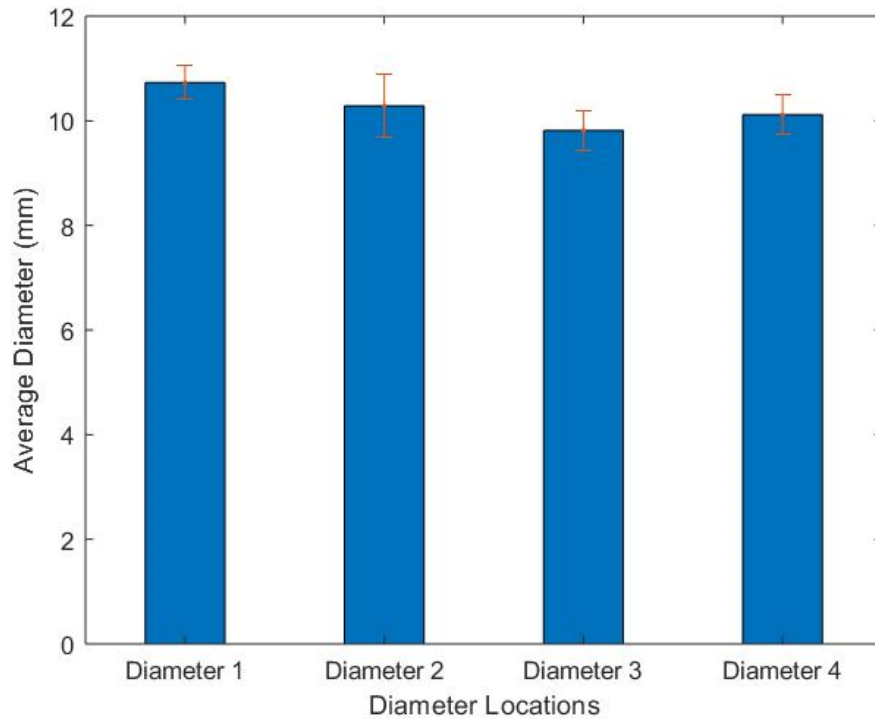


***Figure 38: Average Diameter at each Diameter Location***

Figure 38 illustrates the change in diameter at each diameter location throughout the cylinder. Each diameter theoretically should be 10 mm, but from Figure 28 it is shown that Diameter 1 is slightly bigger than 10 mm and is largest overall diameter while Diameter 3 is slightly smaller than 10 mm and is the overall smallest diameter. While not perfect and slightly different, these measurements show that the cylinder has a diameter roughly 10 mm.

Another complex component produced by the JRLS included a hollow tube with a larger base like that of a vase shown below in Figure 39.



*Figure 39: Hollow Tube with Larger Base*

Figure 39 was included to show that the JRLS is capable of producing more complex prints such as hollow tubes with non-uniform cross-sections.

### **Section 3.6: Measurement and Geometry Shape Validation**

The first shape validation that was completed was the cylinder shown above in Section 3.5. Next the ASTM Standard D638 Type V Dogbone was validated. Figure 40 below illustrates the theoretical shape of the dogbone while Figure 41 displays the measured shape of an actual dogbone print.

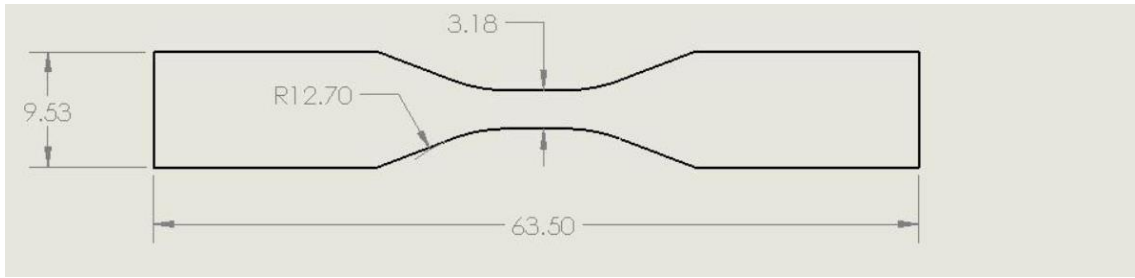


**Figure 40: ATSM Standard D638 Type V Dogbone Dimensions**

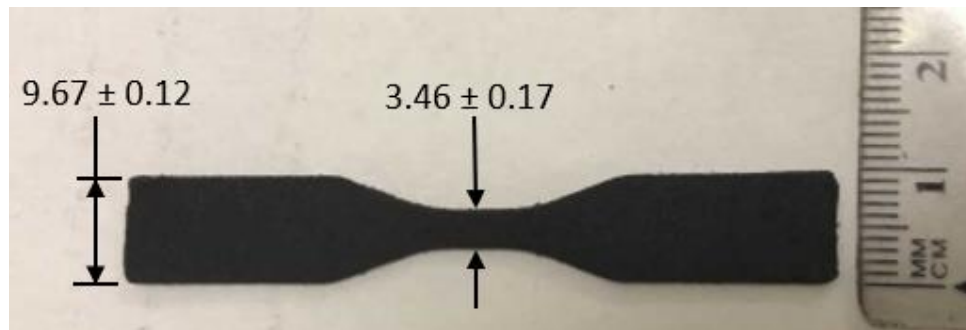


**Figure 41: Dogbone Geometry Measurement**

From Figures 40 and 41, the printed dogbone dimensions are not that far from the theoretical D638 ASTM dimensions. Errors in the dimensions are most likely due to excess powder bonding to the sintered layers caused by excess energy stored in the print dissipating to non-sintered particles during the printing process. Table 6 below reiterates the slight dimension differences shown in Figures 40 and 41.

**Table 6: D638 ASTM Dogbone Dimensions Compared to Printed Dimensions**

	Length (mm)	Width (mm)	Test Section Width (mm)
Theoretical	63.5	9.53	3.18
Actual	63.41 ± 0.29	9.67 ± 0.12	3.46 ± 0.17

While not exact, the dogbone geometry is close to the theoretical shape that is needed for Tensile testing described by the D638 ASTM standards still allowing for useful characterization data. As expected, some error due to the printing parameters and using a laser spot size of 0.2 mm can also be seen.

Along with the shape validation, the thickness of each dogbone sample was also validated.

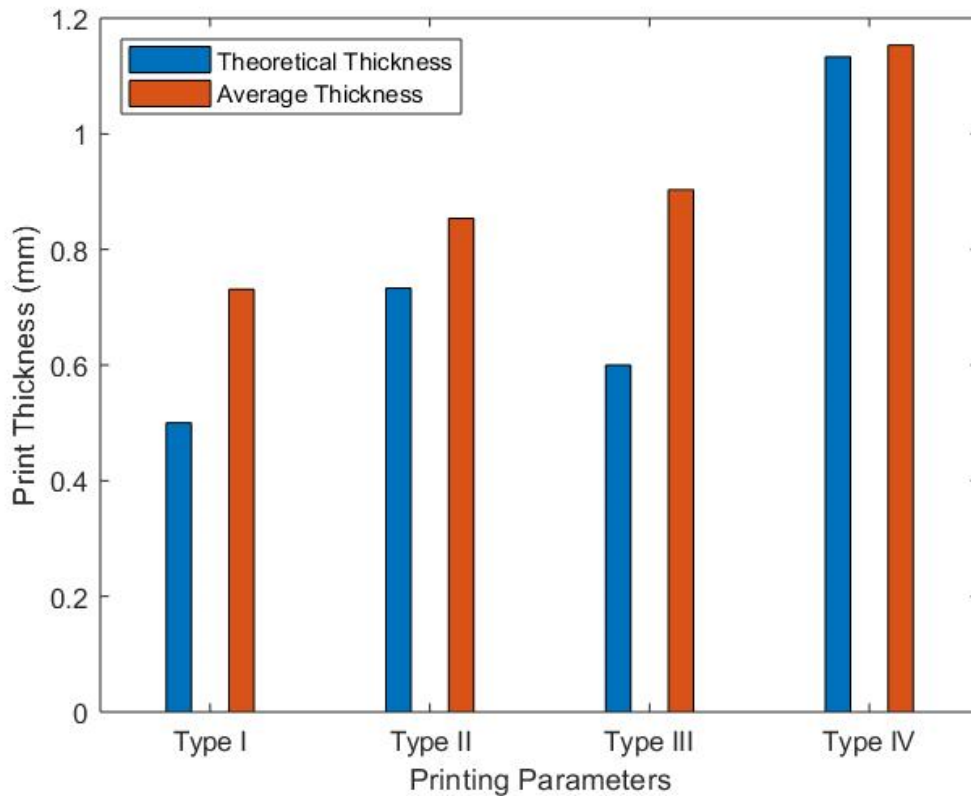


**Figure 42: Average Thickness vs. Print Type**

*Table 7: Thickness Geometry*

Print Type	Average Number of Print Layers	Theoretical Thickness (mm)	Average Thickness (mm)	Margin of Error (mm)
I	$5.0 \pm 0$	0.50	$0.731 \pm 0.092$	0.231
II	$7.5 \pm 0.7071$	0.75	$0.911 \pm 0.016$	0.161
III	$5.5 \pm 0.7071$	0.55	$1.285 \pm 0.014$	0.735
IV	$11.0 \pm 0.7071$	1.10	$1.140 \pm 0.014$	0.04

Figure 42 and Table 7 represent the same data of the comparison of expected theoretical thickness of each printed dogbone sample to the actual measured thickness of each sample. Looking at Figure 42, it can be found that, excluding print Type III again, there is a trend that not only the thickness layer increases with each print type but that also the error of the actual print size to the expected print size decreases. This is later explained in Section 4.2 with Scanning Electron Microscope (SEM) images that each print type increases the uniformity of the print allowing more layers to be printed without curling as well enhancing the print accuracy in terms of thickness. Type III again falls out of this trend due to it not printing in the sintering window. Each sample is slightly larger than its expected theoretical thickness due to the presence porosity and voids found in each sample also seen in the SEM images in Section 4.2. The last take away from Figure 42 and Table 6 is that, besides print Type III, the increase in density or decrease in porosity allows for more precise prints in terms of thickness.

## **Chapter 4: Mechanical Testing of the 3D Printed Samples**

### **Section 4.1: Density Tests**

Due to the irregular shape of the dogbones, density tests were conducted by cutting tiny rectangles from the printed samples and then the volume and mass of these rectangles were recorded. All the dimensions for the volume were measured in millimeters with the width and length of these rectangles being recorded using calipers that had an accuracy of 0.01 mm while the thicknesses of these rectangles were assumed constant and measured using a Rexbeti micrometer with an accuracy of 0.001 mm. The mass of each sample was measured using a very precise scale with 0.001 g accuracy. A picnometer was attempted to measure the densities of the dogbone samples however due to the mass requirement of at least 1 g, the picnometer readings were inaccurate. Other ideas such as water displacement methods were used to measure the volume of the irregular shaped dogbones, however due to the porosity in the sample prints as well as the average sample densities being smaller than the density of water, these attempts were also inaccurate. It is worth noting that the recorded thicknesses of these prints are also slightly inaccurate, even with a very precise tool, because of the porosity and voids present on the surfaces of the HDPE samples causing the readings to be different than the actual true thickness.



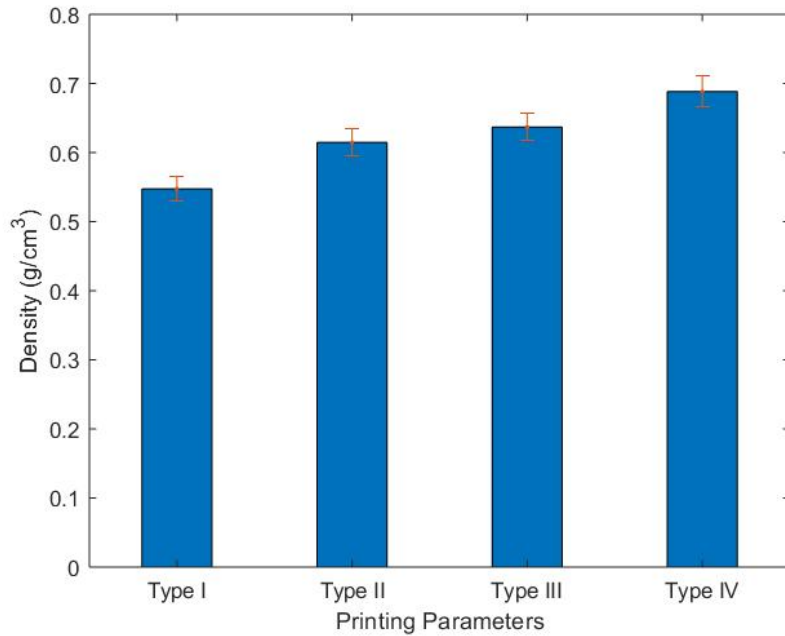


**Figure 43: Average Density with Respect to Printing Type**

**Table 8: Print Type Average Density**

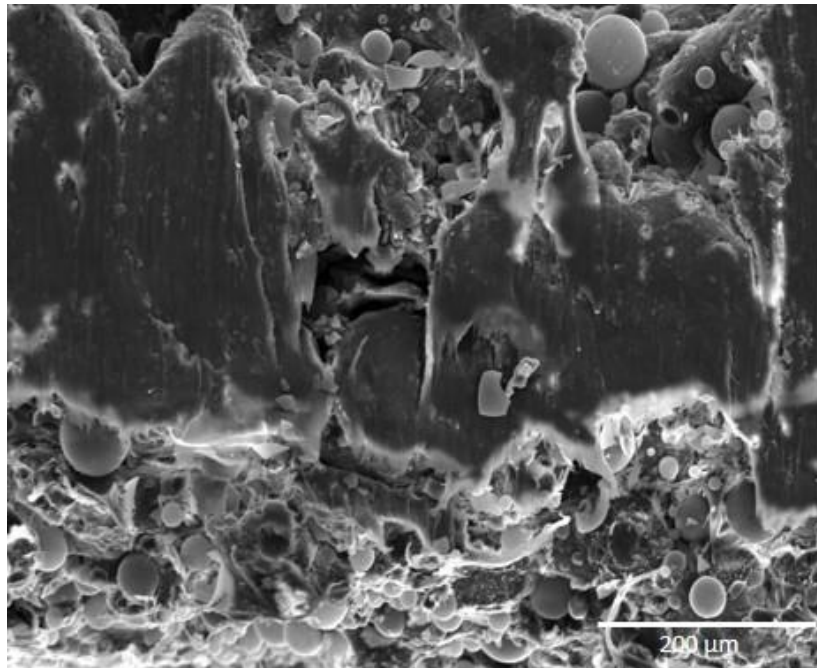
Print Type	Average Density (g/cm <sup>3</sup> )
I	0.548 ± 0.017
II	0.614 ± 0.020
III	0.637 ± 0.020
IV	0.688 ± 0.022

Figure 43 and Table 8 above illustrates the average printed sample densities based off of each different printing type. From the bar graph, each printing type improved in density as the actual density of HDPE is 0.965 g/cm<sup>3</sup>. The main difference in each printing type was the increase in laser power where Type I had the lowest laser power of 3.8 V and Type IV had the highest laser power of 4.4 V. This trend makes sense because as the laser power is increased the powder is heated more causing better bonding between layers. This improvement in bonding between layers caused a decrease in porosity as the density is

slightly enhanced. The true effect of the change in laser intensity can be seen below in Section 4.2 where SEM images were taken of the cross-section of each dogbone.

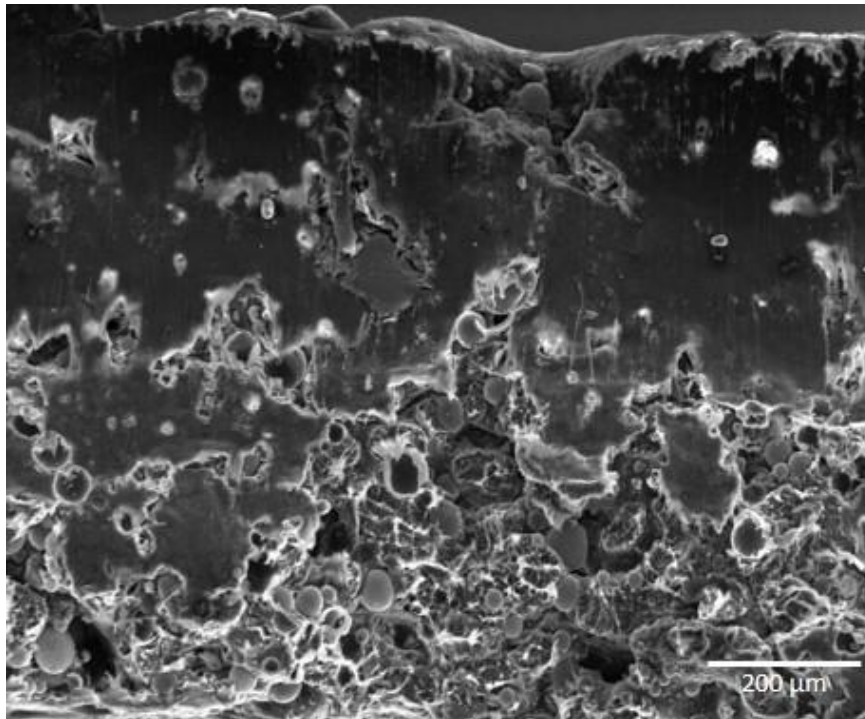
#### **Section 4.2: Scanning Electron Microscope Tests**

A major issue with manufacturing HDPE is the development of porosity and voids in the finished product. SLS in general is known for producing porous parts and using a Scanning Electron Microscope, the porosity and voids present in printed samples and casted samples were compared.



*Figure 44: Print Type I*

The first image taken under the microscope was print Type I shown in Figure 44. This image was taken at 150x magnification at 20 kV. From this image, it is seen that the bottom and top of the sample display bonded layers with loose particles of powder and high porosity as well as a middle streak of well bonded powder and low porosity.



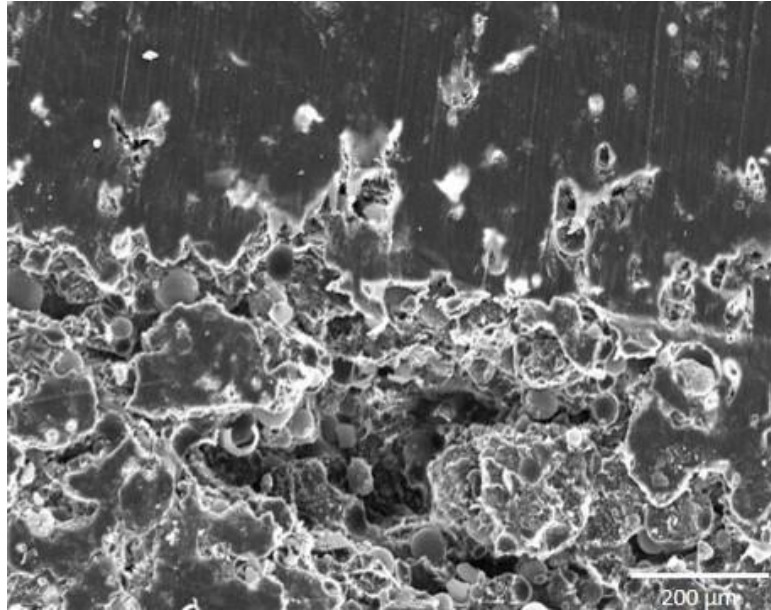
***Figure 45: Print Type II***

Figure 45 shows the SEM image of a Print Type II sample at 100x and 20 kV. Unlike Print Type I, this image shows the top half being better bonded with low porosity and the bottom half with higher porosity and more loose particles of powder rather than a middle streak of high porosity.



*Figure 46: Print Type III*

Figure 46 continues the SEM images with Print Type III. This SEM image shows that nearly the entire sample is melted with low porosity. As later mentioned with more detail in Section 4.3, this is most likely caused by printing process Type III occurring beyond the sintering window after the first few layers, causing the sample to be melted rather than sintered.



*Figure 47: Print Type IV*

Figure 47 lastly displays Print Type IV with about two thirds of the sample not melted with high porosity and the rest slightly melted with low porosity. Unlike the other three print types, Type IV has the least amount of melted region which is a good sign of improvement in terms of printing as the thermal gradient inside this sample is smaller. Because of this smaller melted region, Type IV prints did not curl as much and were able to obtain the largest thicknesses with the most print layers. The last important thing to point out about Figure 47 is that even though the melted region present in the Type IV sample was the smallest, the overall densities of the Type IV prints were still the highest. This means that the overall densities were unaffected by the decrease in melted region which is significant because later in Section 4.3 it will be seen that density plays an important role in the mechanical properties of HDPE.

These SEM images of the HDPE samples are significant because curling and warping in SLS printing is caused by thermal gradients which can be seen in the sample prints through the presence of different melted and sintered regions. Ideally an SLS printed component will have no melted regions and only sintered regions. While this may not result in the most optimal density for a printed component compared to a purely melted casted component, uniformity is extremely important for developing complex prints without any curling and warping. One major key of SLS printed components over mold casting is the ability to create parts with uniform densities due to localized heating rather than density gradients caused by the heat transfer through the molds. The localized heating or energy density ( $E_D$ ) from the laser intensity ( $P$ ), scanning speed ( $SS$ ), layer thickness ( $t$ ), and hatch thickness ( $H$ ) was calculated using Equation 1 below [42].

$$E_D = \frac{P}{SS*t*H} \quad (1)$$

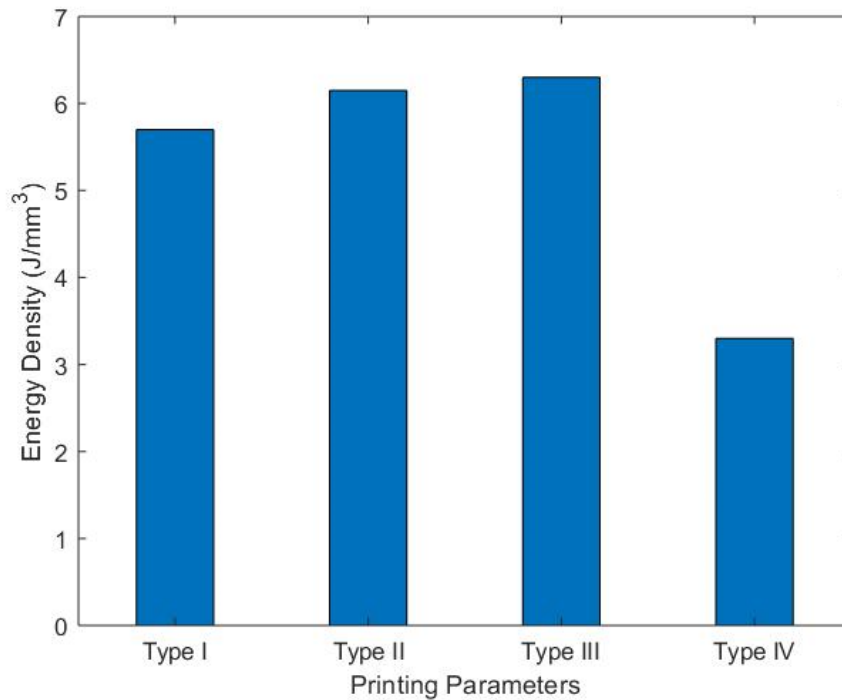


**Figure 48: Energy Density for each Print Type**

**Table 9: Energy Density from Parameters**

Print Type	Laser Power (W)	Energy Density (J/mm <sup>3</sup> )
I	0.570	5.70
II	0.615	6.15
III	0.630	6.30
IV	0.660	3.30

Figure 48 and Table 9 above display the energy that is portrayed onto the powder for each print type parameters assuming a 0.1 mm layer thickness and 0.1 mm hatch thickness. Following the SEM images and density calculations, it can be seen that energy density follows the trend of growing uniformity in the prints as the energy density approaches the sweet spot in the sintering window. Type III, which has the largest energy, also has the largest melted region meaning that the perfect energy density needed to eliminate non-uniform printing and curling is closer to the energy density in Type IV as it has the smallest melted region. Type IV can also be assumed closer to the most optimal energy density for sintering HDPE as it produces a higher overall print density even though it provides the lowest amount of energy per volume.

Using the known HDPE powder density ( $\rho_{\text{powder}}$ ) of 0.965 g/cm<sup>3</sup> given by the powder data sheet and the print densities ( $\rho_{\text{print}}$ ), the average percentage of voids in each print and casted type were calculated using Equation 2 and presented in Table 10 below.

$$\text{Void Percentage} = \left[ 1 - \frac{\rho_{\text{print}}}{\rho_{\text{powder}}} \right] (100) \quad (2)$$

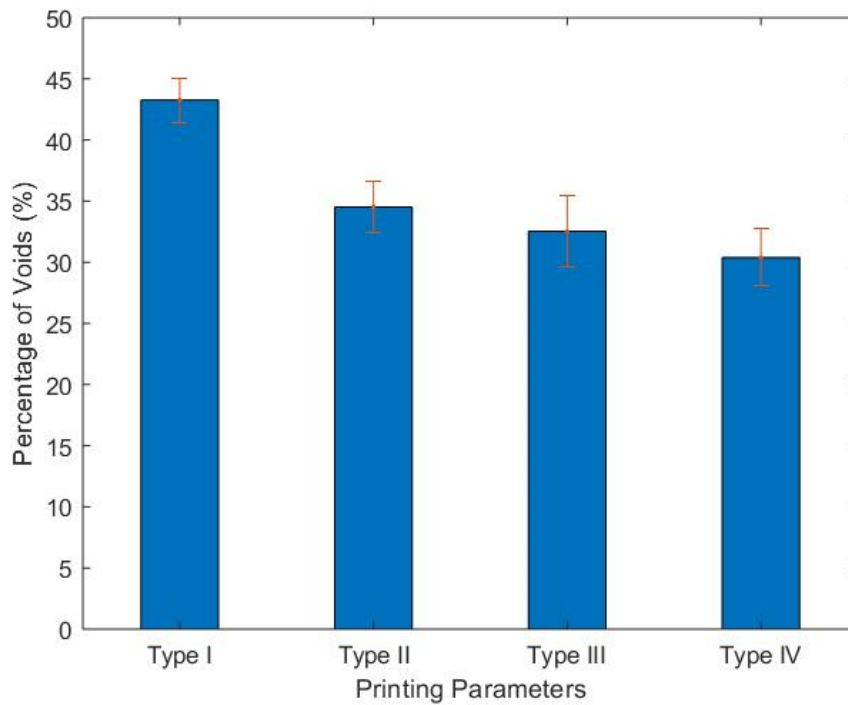


**Figure 49: Percentage of Voids**

**Table 10: Percentage of Voids**

	Percentage of Voids (%)
Type I	43.264 ± 1.799
Type II	34.522 ± 2.070
Type III	32.522 ± 2.931
Type IV	30.389 ± 2.326

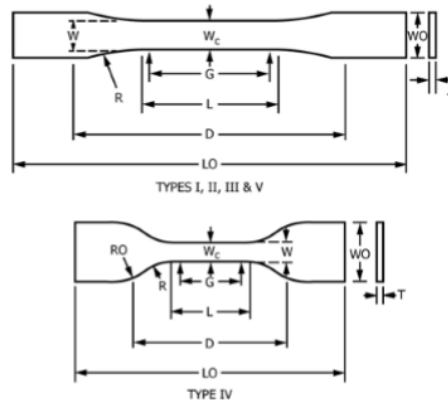
The trend in Table 10 follows the similar trend seen in Figure 49 where the percentage of voids decreases as the density of each printing type increases. Type IV had the best the percentage of void as it was the smallest of the group with roughly only 30% voids.

### **Section 4.3: Tensile Tests Results of SLS Printed Samples**

In this section, tensile testing involving ASTM D638 standards and ASTM D882 standards were conducted. Both standards were used with Type V dogbones with



guidelines and dimensions shown in Figure 50 below. D882 standards were used with dogbones with thicknesses less than 1 mm and D638 standards were used with dogbones with thicknesses greater than 1 mm [43].



Specimen Dimensions for Thickness,  $T$ , mm (in.)<sup>A</sup>

Dimensions (see drawings)	7 (0.28) or under		Over 7 to 14 (0.28 to 0.55), Incl	4 (0.16) or under		Tolerances
	Type I	Type II	Type III	Type IV <sup>B</sup>	Type V <sup>C,D</sup>	
$W$ —Width of narrow section <sup>E,F</sup>	13 (0.50)	6 (0.25)	19 (0.75)	6 (0.25)	3.18 (0.125)	$\pm 0.5$ ( $\pm 0.02$ ) <sup>B,C</sup>
$L$ —Length of narrow section	57 (2.25)	57 (2.25)	57 (2.25)	33 (1.30)	9.53 (0.375)	$\pm 0.5$ ( $\pm 0.02$ ) <sup>C</sup>
$WO$ —Width overall, min <sup>G</sup>	19 (0.75)	19 (0.75)	29 (1.13)	19 (0.75)	...	+ 6.4 (+ 0.25)
$WO$ —Width overall, min <sup>G</sup>	...	...	...	...	9.53 (0.375)	+ 3.18 (+ 0.125)
$LO$ —Length overall, min <sup>H</sup>	165 (6.5)	183 (7.2)	246 (9.7)	115 (4.5)	63.5 (2.5)	no max (no max)
$G$ —Gage length <sup>I</sup>	50 (2.00)	50 (2.00)	50 (2.00)	...	7.62 (0.300)	$\pm 0.25$ ( $\pm 0.010$ ) <sup>C</sup>
$G$ —Gage length <sup>I</sup>	...	...	...	25 (1.00)	...	$\pm 0.13$ ( $\pm 0.005$ )
$D$ —Distance between grips	115 (4.5)	135 (5.3)	115 (4.5)	65 (2.5) <sup>J</sup>	25.4 (1.0)	$\pm 5$ ( $\pm 0.2$ )
$R$ —Radius of fillet	76 (3.00)	76 (3.00)	76 (3.00)	14 (0.56)	12.7 (0.5)	$\pm 1$ ( $\pm 0.04$ ) <sup>C</sup>
$RO$ —Outer radius (Type IV)	...	...	...	25 (1.00)	...	$\pm 1$ ( $\pm 0.04$ )

**Figure 50: Standard D638 Type V Dogbone dimensions [44]**

Figure 50 above describes the exact dimensions of the Type V dogbones that were modeled in CAD and printed for this study. The geometry validation of the printed dogbones were discussed previously in Section 3.6. Based on the ASTM standard, the Type V dogbones in this study were tested using The University of Oklahoma’s Instron 3345 Machine with the grips placed 25.4 mm (1 in) apart and ran at 1 mm/min shown in Figure 51 below [44].

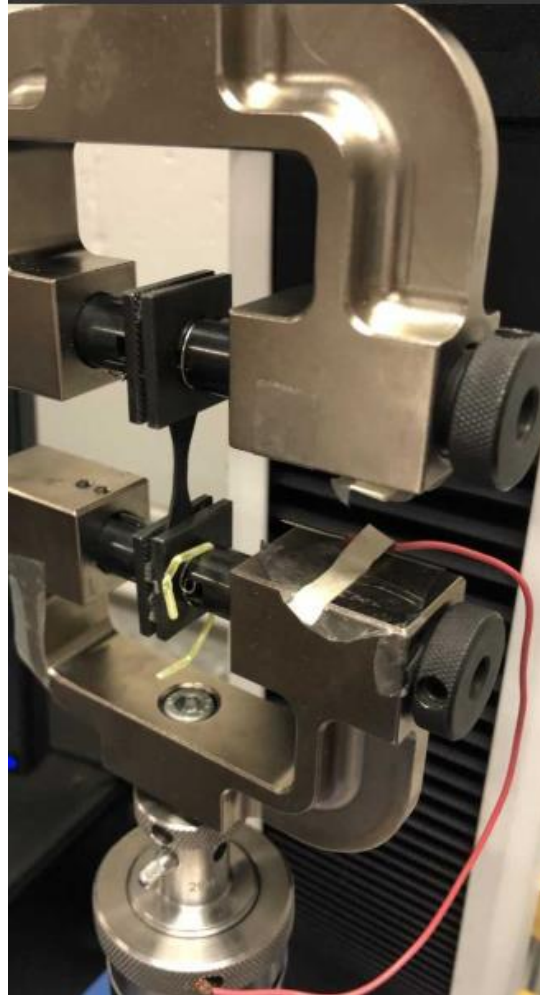


***Figure 51: Instron Tensile Testing Setup***

As shown in Figure 51, each dogbone specimen was secured to an upper and lower actuator with gripping clamps. Running the tests at 1 mm/min, a 100 N load cell was used while the load and extension of the dogbones until fracture was recorded. To get the stress-strain data, the test section width and thickness of each dogbone sample was also recorded before each test. The stress of each sample was calculated using the equation

$$\sigma = \frac{Load}{Area} \quad (3)$$

where load was recorded with the Instron machine and the area of the test section was measured prior to testing using calipers for the width and a Rexbeti measurement instrument for the thickness. The strain of each sample was calculated with the equation

$$\varepsilon = \left[ \frac{\Delta l}{l} \right] * 100 \quad (4)$$

where change in length was recorded by the Instron machine and the original length of 25.4 mm was preset as the distance between the grips. Finally, the modulus of elasticity was measured using the standard slope equation

$$m = \frac{\Delta y}{\Delta x} \quad (5)$$

where the change in Y represents the change in strain from 0 to 0.1% strain and the change in X represents the change in stress from 0 to 0.1% strain. 0.1% strain was chosen as all samples displayed linearity from this range in the sample data following Hooke's Law.

The first stress-strain curve gathered from tensile testing involved the Type I printed samples and can be seen in Figure 52 below.

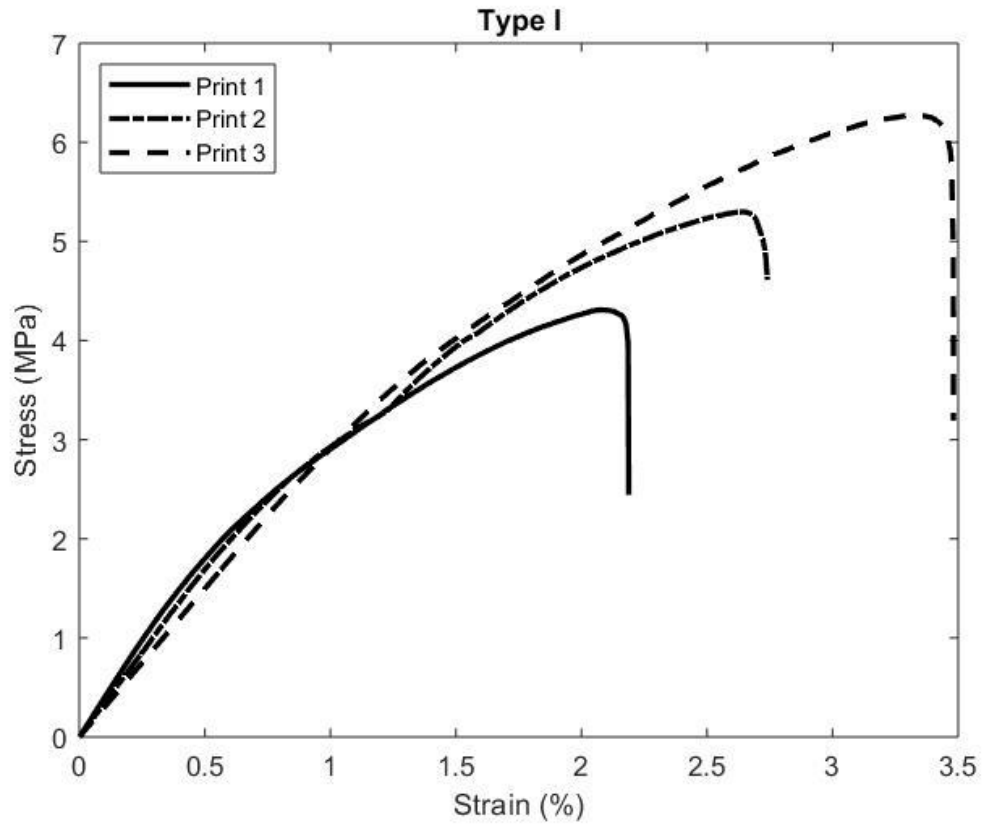


***Figure 52: Type I Print Stress Strain Curve***

Figure 52 illustrates the results of the three best Type I printed samples. From this figure, it can be seen that the best stress and strain came from Print 3 as it obtained the largest stress around 6 MPa and also the largest strain around 3.5% before failure.

The next stress-stain curve taken from the Instron tensile testing were the Type II printed dogbone samples shown in Figure 53 below.

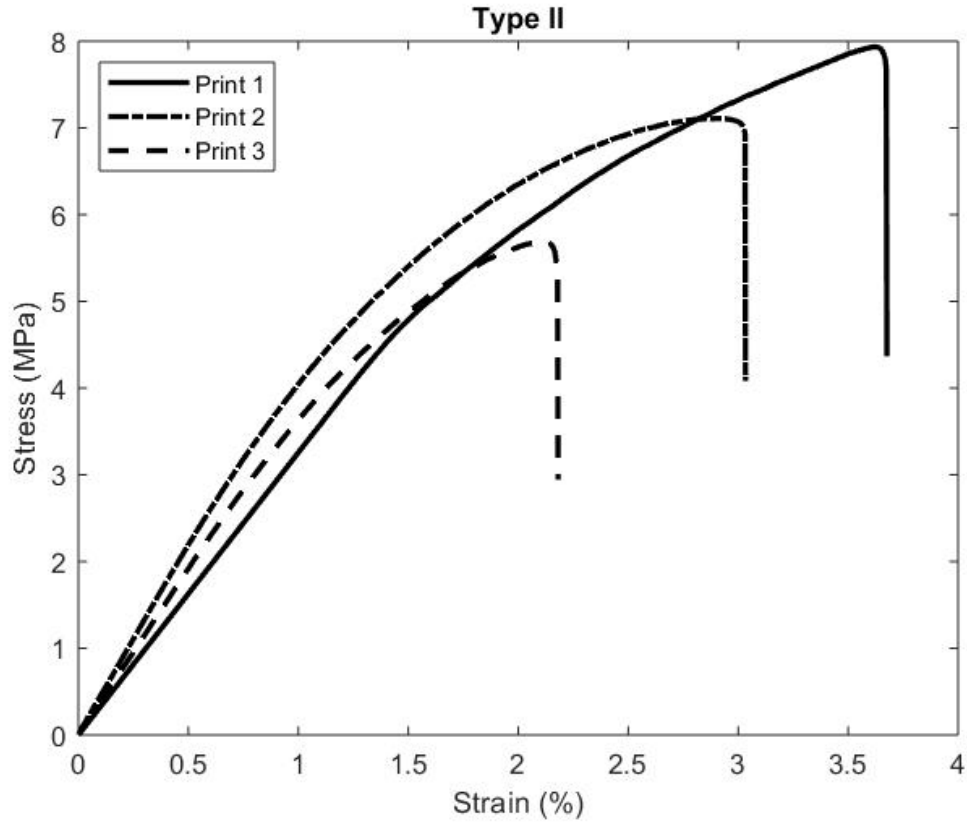


***Figure 53: Print Type II Stress Strain Curve***

It can be seen immediately from Figure 53 that the Type II printed samples were better in terms of stress as the lowest print, Print 3, had almost the same maximum stress as the lowest Type I print because of the increase in density and thickness. It is interesting to point out that while the stress was improved with the Type II printing method, the strain however stayed relatively the same as the Type I strain with the maximum strain also occurring around 3.5%.

Unlike the stress improvement seen from printing Type I to II, printing Type III displayed similar maximum stress as Type II.

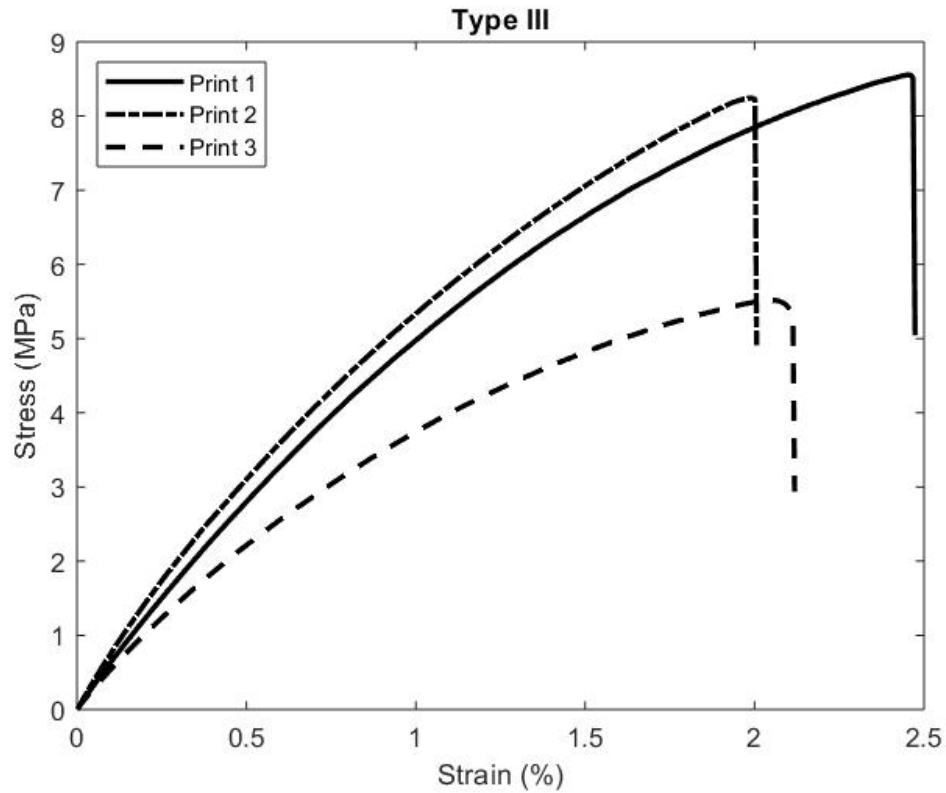


*Figure 54: Print Type III Stress Strain Curve*

Along with this observation, it can also be pointed out from Figure 54 that the maximum strain of printing Type III is decreased from the maximum strain of both printing Types I and II at just a maximum strain of 2.5%.

The results of printing Type IV, shown in Figure 55, proved to have the best maximum stress as its best print, Print 1, reached a maximum stress over 12 MPa.

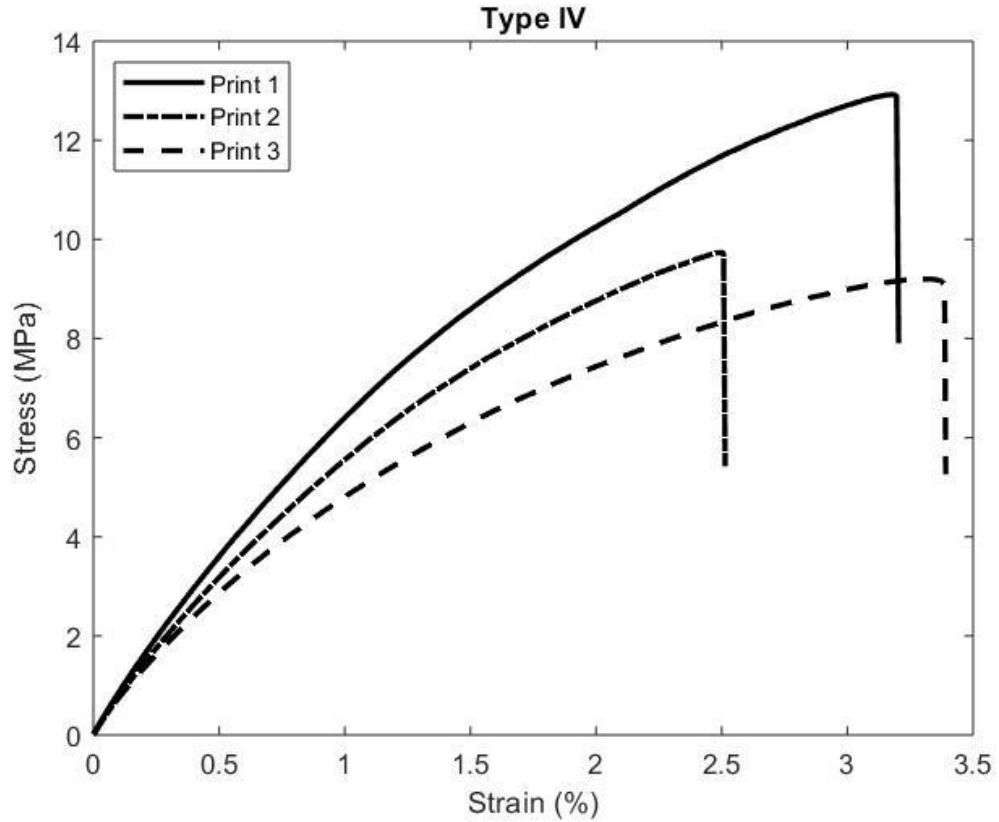


**Figure 55: Print IV Stress Strain Curve**

While printing Type IV had the best stress, its maximum strain on the other hand was slightly lower than both printing Types I and II as the maximum strain attained was just under 3.5%.

**Table 11: Comparison of Maximum Stress, Strain, and Modulus**

	Average Maximum Stress (MPa)	Average Maximum Strain (%)	Average Modulus (MPa)
Type I	$5.294 \pm 0.983$	$2.697 \pm 0.631$	$3.472 \pm 0.515$
Type II	$5.421 \pm 0.410$	$2.146 \pm 0.250$	$3.815 \pm 0.570$
Type III	$7.439 \pm 1.670$	$2.163 \pm 0.254$	$6.440 \pm 1.121$
Type IV	$10.619 \pm 2.012$	$3.001 \pm 0.439$	$7.637 \pm 0.678$

Table 11 above averages the maximum stress, maximum strain, and modulus of the three best prints from each printing type shown in Figures 52-55. It can be seen from this table that while the maximum individual print stress of each printing type did not necessarily have a positive trend, the average maximum stress of each printing type did have a positive trend as printing Type IV had the superior maximum average stress. Another slight difference from the overall maximum strain trend of each type's best individual prints, Type IV again had the highest averaged maximum strain followed by printing Type I. The modulus, while not present in Figures 52-55, can be seen in Table 11 with a positive trend from printing Type I to printing Type IV with Type IV again having the highest average modulus.

The improvements in stress and modulus with each print type indicate that an increase in density and thickness directly influence the mechanical properties of SLS printed HDPE. Each printing type was developed to enhance the preceding print type's density and number of layers (thickness) that could be printed successfully without curling. Going even farther, the laser intensity and scanning speed of each printing type directly affect the changes in density and thickness of each print and therefore are the true influencers of mechanical property enhancements witnessed throughout each printing type. Table 12 below was inserted to show the increases in density and thicknesses throughout the printing types that influence the enhancement in stress and modulus.



**Table 12: Average Density and Thickness of Each Print Type**

	Average Density (g/cm <sup>3</sup> )	Average Thickness (mm)
Type I	0.548 ± 0.017	0.731 ± 0.092
Type II	0.632 ± 0.020	0.854 ± 0.099
Type III	0.651 ± 0.028	0.903 ± 0.108
Type IV	0.672 ± 0.022	1.153 ± 0.025

Table 12 explains why the stress and modulus increase throughout each printing type however it does little to explain why the strain decreases from Type I to Type II and III but then increases again in Type IV. Not shown in Table 12 is the amount of curling and warping that printing Type II and III experienced causing their prints to fail earlier than the other types. Out of all four types, these two were by far the worst most likely due to sintered outside of the sintering window. It is likely that printing Type II and III are outside the sintering window due to the large number of melted particles seen in the SEM images as well as the large presence of curling on the dogbone edges. While printing Types II and III improve density and thickness, which also improve the stress and modulus, the strain is most likely lessened due to the thermal gradient and thermal shock experienced by the samples during the printing process.

#### **Section 4.4: Printed Sample Tensile Test Results Compared with Casted Samples**

After completing the tensile testing results of the printed samples, these samples were then compared to tensile testing results of casted samples. The casted samples were created with two aluminum molds with similar D638 ASTM Type V dimensions shown in Figure 56 below.

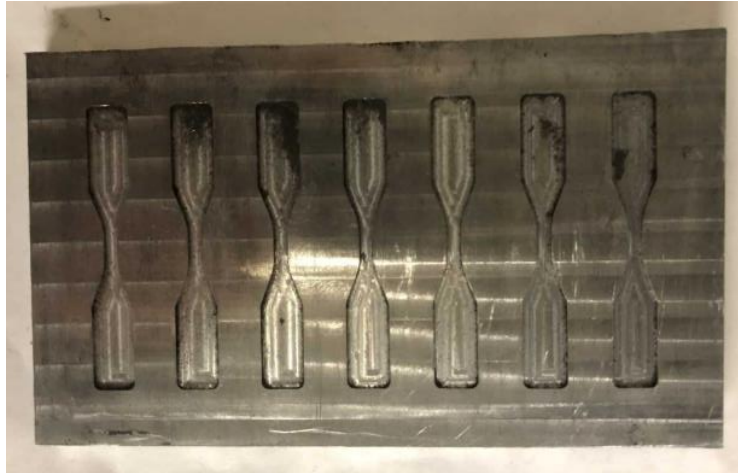


***Figure 56: Casted Sample Mold***

Figure 56 displays the molds that were used for each casted and placed into an oven at 160°C. The first set of casted samples, referred to as Casted I, were placed into an aluminum mold with a 3 mm thickness depth and the second set of casted samples, referred to as Casted II, were placed into an aluminum mold except with only a 1 mm thickness. Both thicknesses were used to model all four types of printed samples with varying thicknesses. The Casted I samples were placed into an oven at 160°C for 30 minutes and the Casted II samples were placed into the same oven at 160°C for only 10 minutes. Both molds had lids with indents in them allowing for the powder to compact before being placed in the oven. The length of time in the oven for both sample sets were determined by the minimum time that the powder melted together as the purpose of the casted samples were to get their densities and thicknesses as close to the printed densities and thickness as possible for comparison.

Figures 57 and 58 compare the casted densities and thicknesses with the densities and thicknesses of each printing type.

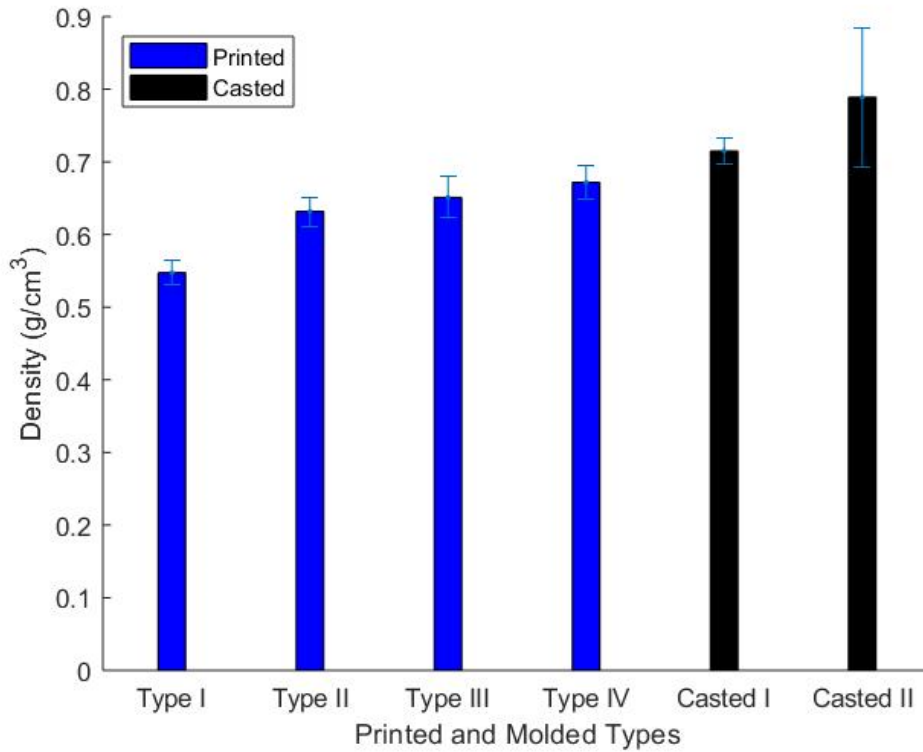


***Figure 57: Printed vs. Casted Average Density***

From Figure 57, both Casted I and Casted II samples have an average higher density than all four of the printing type densities. This is expected because the powder was compacted down inside of the molds as well as the oven being incapable of localizing heat like a laser and therefore having to melt rather than sinter the samples to bond them. The result of the oven melting the powder into the casted shape is that both sets of casted samples have higher densities than the printed samples. Casted II is seen to have a larger density than Casted I most likely due to the smaller thickness of Casted II's mold, resulting in more compact particles inside a smaller space as well as less powder needing to heat up before bonding.

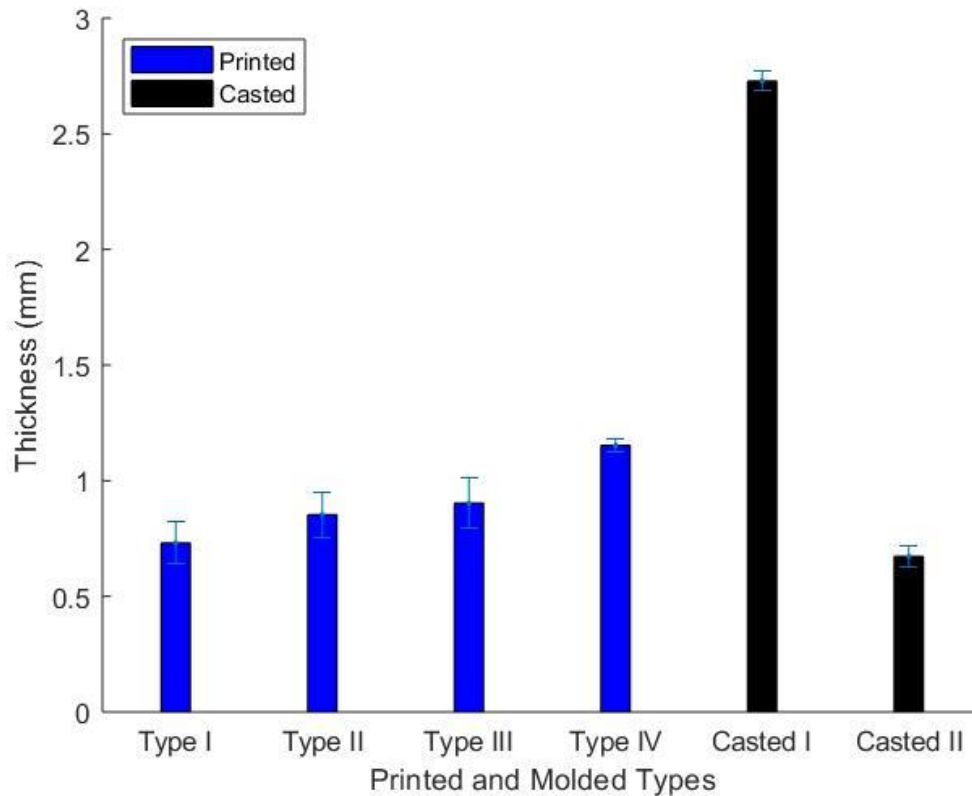


**Figure 58: Printed vs. Casted Average Thickness**

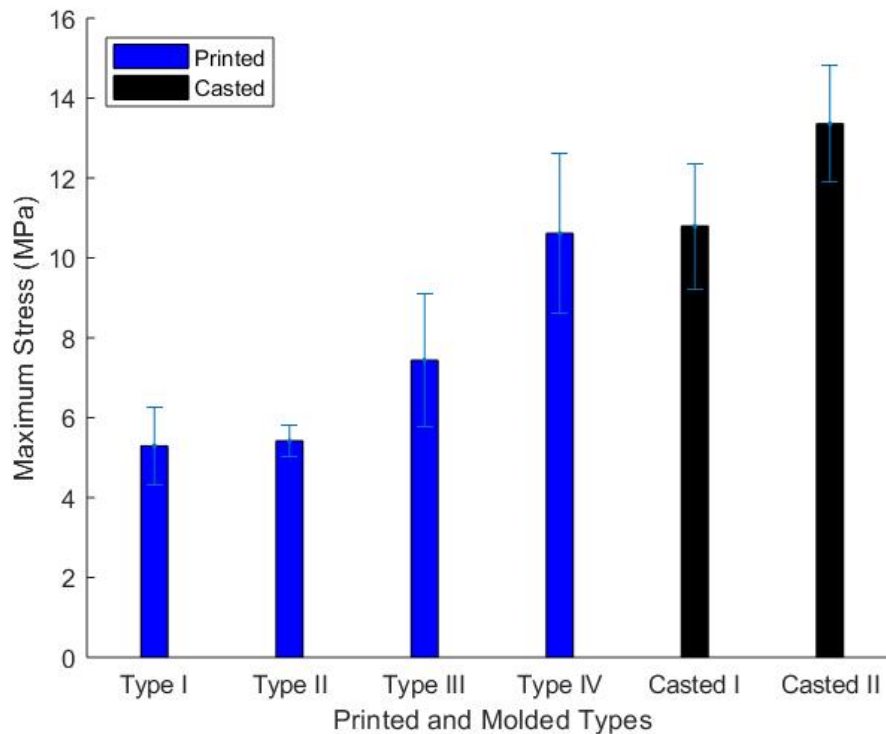
As mentioned at the beginning of this section, Casted I’s mold had a thickness of 3 mm and Casted II’s mold had a thickness of 1 mm. Figure 58 displays that Casted I had the largest thickness as expected from the large thickness of its mold, and Casted II had an average thickness smaller than even the average thickness of print Type I. Both casted thicknesses however are significantly smaller than the expected thicknesses of 3 mm and 1 mm caused by the melting that takes place during the casting process. Already the comparison of thicknesses shows that the thickness accuracy of SLS printing is superior to the thickness accuracy of mold casting around the same density as less melting and shrinkage takes place during the printing process than the casting process.

Table 13 represents the comparison of printed and casted samples summarized by Figures 57 and 58.

**Table 13: Printed vs. Casted Density and Thickness**

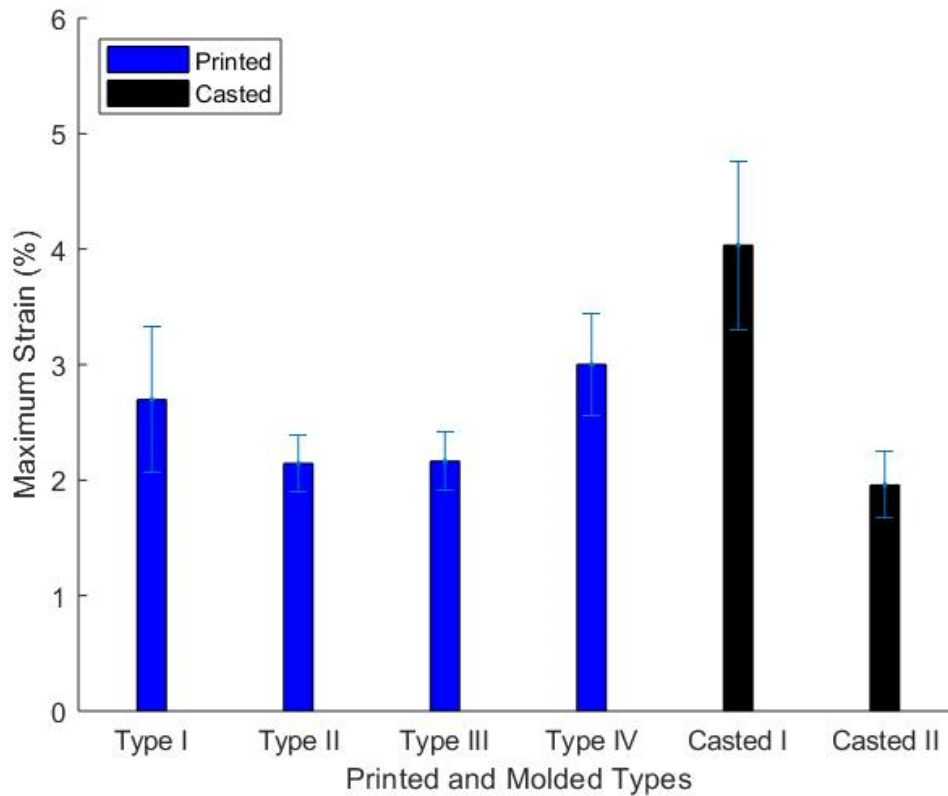
	Average Density (g/cm <sup>3</sup> )	Average Thickness (mm)
Type I	0.548 ± 0.017	0.731 ± 0.092
Type II	0.6321 ± 0.020	0.854 ± 0.099
Type III	0.651 ± 0.028	0.903 ± 0.108
Type IV	0.672 ± 0.022	1.153 ± 0.025
Casted I	0.715 ± 0.017	2.729 ± 0.042
Casted II	0.789 ± 0.095	0.673 ± 0.049

Table 13 again shows the trend of increasing density and plotted thicknesses represented in Figures 57 and 58 that are the main parameters that can be controlled in both SLS printing and mold casting.



**Figure 59: Printed vs. Casted Average Maximum Stress**

When comparing the maximum stress, Figure 59 again shows that increasing the density also increases the stress. Because of this, it is not of much surprise that the casted samples are stronger in terms of stress than the printed samples. However, this leads to the conclusion that if the printed samples were able to obtain similar densities then they would be just as strong if not stronger than the casted samples.



**Figure 60: Printed vs. Casted Average Maximum Stress**

From Figure 60, it can be seen that Casted I has a much larger strain than any printed sample as well as Casted II. Similar to the lack of a trend that was present in the printed samples, the casted samples also do not follow a clear strain trend based off of density. However, when ignoring print Type II and III, which may give bad strain data

due to being outside the sintering window, there is in fact a trend with thickness. This trend shows that as the thickness increases so does the strain.

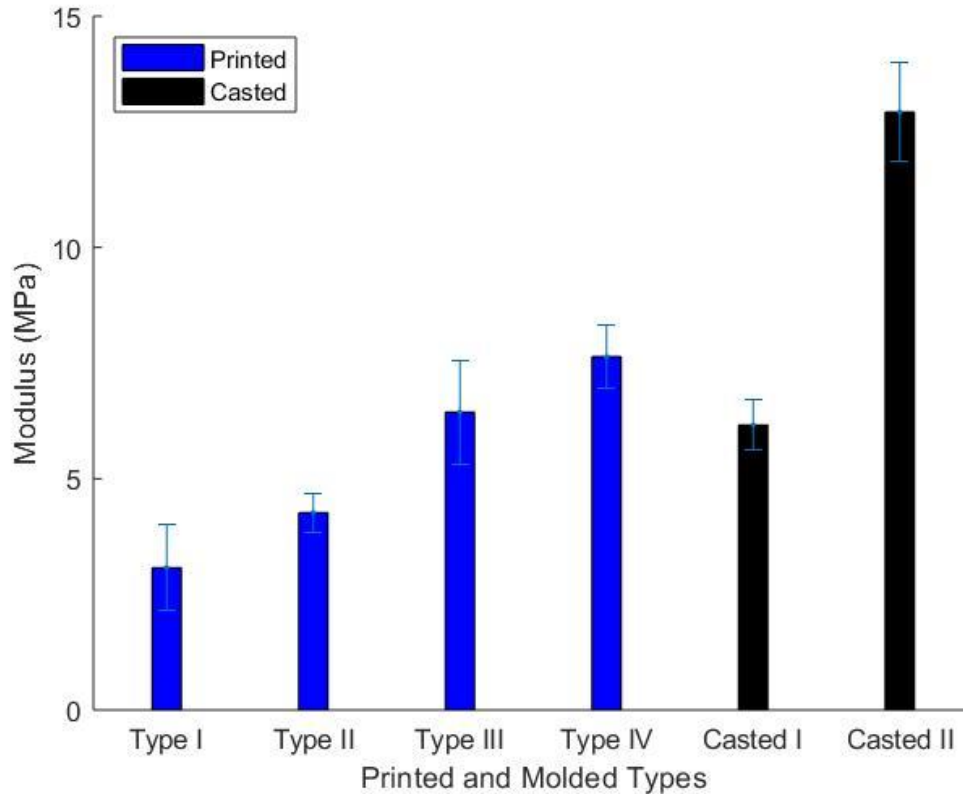


**Figure 61: Printed vs. Casted Average Maximum Stress**

While it was shown with the comparison of stress that an increase in density also resulted in an increase in stress, Figure 61 displays that this is almost true for modulus. Casted II continues this trend, however the modulus of Casted I is actually weaker than both the modulus of print Types III and IV. This may just be an outlier but never the less it is seen that around a density  $0.7 \text{ g/cm}^3$  the SLS printing process produces a stronger modulus than the molded casting process.

Table 14 below represents the comparison of printed and casted samples summarized by Figures 58-61.

**Table 14: Printed vs. Casted Stress, Strain, and Modulus**

	Average Max Stress (MPa)	Average Max Strain (%)	Average Modulus (MPa)
Type I	5.294 ± 0.983	2.697 ± 0.631	3.472 ± 0.515
Type II	5.421 ± 0.410	2.146 ± 0.250	3.815 ± 0.570
Type III	7.440 ± 1.670	2.163 ± 0.254	6.440 ± 1.121
Type IV	10.619 ± 2.012	3.001 ± 0.439	7.640 ± 0.678
Casted I	10.799 ± 1.567	4.033 ± 0.730	6.162 ± 0.534
Casted II	13.358 ± 1.469	1.958 ± 0.289	12.927 ± 1.073

Table 14 reiterates the comparisons made between the stress, strain, and modulus of both the printed and casted samples. This table, and Table 11, illustrate the trend that an increase in density increases both the stress and modulus. This table can also be used to see the trend between the strain of Print Type I, Print Type IV, Casted I, and Casted II and thickness that as the thickness increases so does the strain.

The purpose of this thesis was to compare affordably printed SLS HDPE with casted samples. Overall, it can be seen that SLS printing and mold casting both have their pros and cons. SLS printing can result in more accurate component dimensions with similar mechanical properties at specific densities, however mold casting can be used to create quicker parts that achieve an overall higher density and higher thickness [45]. From the results, casted samples are still stronger in terms of stress but Casted I is weaker than Type IV in terms of strain and modulus. These results show that stress and modulus are directly proportional to having higher density. Casted II on the other hand, while having the strongest stress and modulus, has the weakest strain. This shows that strain is more



dependent on the thickness of the sample rather than density as Casted I, which is the thickest sample, has the largest strain.

## **Chapter 5: Conclusions and Future Work**

The mechanical properties and density of HDPE developed through selective laser sintering and casted molding were compared and studied. In order to obtain results, an affordable SLS 3D Printer was developed specifically for the additive manufacturing of HDPE. The JRLS was designed to have a controllable ambient temperature, bed temperature, laser intensity, and laser scanning speed as these parameters were found to be the most important for properly printing HDPE. It was also found that these four parameters were the key to eliminating curling in HDPE prints as these allowed for each layer of the print to stay uniform and inside the sintering window. Four different printing types and two different casted mold types were tested and compared. The four different printing types were tested using the four main parameters at different settings and the two casted mold types had different oven times at 160°C and thicknesses of 1 mm and 3 mm. The casted samples were prepared specifically to model the densities and thicknesses of the printed samples. All samples were tested on an Instron 3345 machine using either ASTM D638 standards or ASTM D882 standards. Results concluded that higher densities increased both the stress and modulus of all the HDPE samples and higher thicknesses in Print Type I, Print Type IV, Casted I, and Casted II improved the strain. In terms of the processes, SLS printing proved to be much more accurate for the thicknesses of the developed samples however, casting HDPE proved to be much quicker than printing while also allowing for thicker and denser samples. At similar densities, results showed that the mechanical properties were similar for both printed and casted samples however, casted samples were able to produce samples with the highest density and overall best mechanical properties.

Improving the printing process of HDPE in terms of thickness and density would allow for printed samples with similar mechanical properties to casted samples. The density of SLS can be maximized by printing at the highest temperature inside the sintering window allowing for the maximum amount of bonding during the printing process with little to no curling or warping. It was found in this study that it is much easier to print samples with small cross-sectional areas and one idea to improve the thickness of the printed samples would be to print the dogbone samples vertically. While this method is not the most efficient in terms of powder usage, this method would theoretically allow for samples to be printed at the desired thickness with less curling because of the smaller cross-sections. Further work needs to be completed to see if this option is viable in retaining the promising mechanical properties found from printing dogbones horizontally.

Print Type IV was the best all-around printing type and is a good starting point for improving SLS printing of HDPE. The main issue with Type IV is that if larger surface area prints are desired then curling becomes an issue after 12 or so layers. From the SEM images, it was shown that Type IV samples still had a few melted layers and to eliminate curling, all layers need to be uniform. As the prints get deep into layers, the entire part seems to be heating up until some point where the print is too hot, and the top layers are melting because of it. Future work can build off print Type IV's parameters to find the perfect heat balance to have every layer uniform. One idea that is currently being tested is decreasing the heat in the later layers that are experiencing this melting. The two different methods attempting to solve this issue are speeding up the scanning speed or manually decreasing the laser intensity during these later layers. Currently this method has given promising results as more layers are able to be produced than with Type IV. The largest

prints from this method have followed the format of printing at 4.4 V while increasing the scanning speed 1 mm/s every layer starting at 20 mm/s. Density and mechanical tests still need to be completed for this method.

More work can also be done on the theoretical side involving hot stage microscopy (HSM) and heat transfer calculations about the heat and energy absorbed by each layer of powder [46], [47]. This method would prevent curling by printing with the exact amount of heat and energy needed to stay in the sintering window, eliminating the trial and error approach completely [48]. Ideally this method would allow calculated approaches for setting the laser intensity, scanning speed, ambient temperature, and the bed temperature at the specific settings eliminating the trial and error approach shown in the four printing types described in this study.

Other future work with HDPE should be the addition of nanoparticles such as Carbon Nanotubes (CNTs) mixed with HDPE powder to print conductive parts with piezoelectric properties and enhanced mechanical properties [49], [50]. These prints will allow for complex sensors to be printed and tested in terms of conductivity, resistivity, and mechanical properties.

## References

1. Rostek, J., *JRLS 1000 DIY SLS-3D-PRINTER*. 2016.
2. Schmid, M., A. Amado, and K. Wegener. *Polymer powders for selective laser sintering (SLS)*. in *AIP Conference proceedings*. 2015. AIP Publishing.
3. Technologies, A.C.F.o.A.M. and A.C.F.o.A.M.T.S.F.o. Terminology, *Standard terminology for additive manufacturing technologies*. 2012: ASTM International.
4. Jasiuk, I., et al., *An overview on additive manufacturing of polymers*. JOM, 2018. **70**(3): p. 275-283.
5. Paesano, A., *Polymeric Additive Manufacturing: Present Status and Future Trends of Materials and Processes*. 2016, Boeing.
6. Wohlers, T., *Wohlers Report 2017*. USA: Wohlers Associates. 2017, Inc.
7. Gao, W., et al., *The status, challenges, and future of additive manufacturing in engineering*. Computer-Aided Design, 2015. **69**: p. 65-89.
8. Lieneke, T., et al., *Dimensional tolerances for additive manufacturing: Experimental investigation for Fused Deposition Modeling*. Procedia CIRP, 2016. **43**: p. 286-291.
9. N. Turner, B., R. Strong, and S. A. Gold, *A review of melt extrusion additive manufacturing processes: I. Process design and modeling*. Rapid Prototyping Journal, 2014. **20**(3): p. 192-204.
10. Calignano, F., et al., *Overview on Additive Manufacturing Technologies*. Proceedings of the IEEE, 2017. **105**(4): p. 593-612.

11. Dawoud, M., I. Taha, and S.J. Ebeid, *Mechanical behaviour of ABS: An experimental study using FDM and injection moulding techniques*. Journal of Manufacturing Processes, 2016. **21**: p. 39-45.
12. Weng, Z., et al., *Mechanical and thermal properties of ABS/montmorillonite nanocomposites for fused deposition modeling 3D printing*. Materials & Design, 2016. **102**: p. 276-283.
13. Chohan, J.S., et al., *Dimensional accuracy analysis of coupled fused deposition modeling and vapour smoothing operations for biomedical applications*. Composites Part B: Engineering, 2017. **117**: p. 138-149.
14. Casavola, C., et al., *Residual stress measurement in fused deposition modelling parts*. Polymer Testing, 2017. **58**: p. 249-255.
15. Gross, B.C., et al., *Evaluation of 3D printing and its potential impact on biotechnology and the chemical sciences*. 2014, ACS Publications.
16. Cooke, M.N., et al., *Use of stereolithography to manufacture critical-sized 3D biodegradable scaffolds for bone ingrowth*. Journal of Biomedical Materials Research Part B: Applied Biomaterials: An Official Journal of The Society for Biomaterials, The Japanese Society for Biomaterials, and The Australian Society for Biomaterials and the Korean Society for Biomaterials, 2003. **64**(2): p. 65-69.
17. Pan, Y. and Y. Chen, *Meniscus process optimization for smooth surface fabrication in Stereolithography*. Additive Manufacturing, 2016. **12**: p. 321-333.
18. Choong, Y.Y.C., et al., *4D printing of high performance shape memory polymer using stereolithography*. Materials & Design, 2017. **126**: p. 219-225.

19. Choi, J.-W., H.-C. Kim, and R. Wicker, *Multi-material stereolithography*. Journal of Materials Processing Technology, 2011. **211**(3): p. 318-328.
20. Wu, X., et al., *Tilting separation analysis of bottom-up mask projection stereolithography based on cohesive zone model*. Journal of Materials Processing Technology, 2017. **243**: p. 184-196.
21. Liu, T., et al., *Microstructural defects induced by stereolithography and related compressive behaviour of polymers*. Journal of Materials Processing Technology, 2018. **251**: p. 37-46.
22. Vdovin, R., et al., *Implementation of the additive PolyJet technology to the development and fabricating the samples of the acoustic metamaterials*. Procedia Engineering, 2017. **176**: p. 595-599.
23. Ibrahim, D., et al., *Dimensional error of selective laser sintering, three-dimensional printing and PolyJet™ models in the reproduction of mandibular anatomy*. Journal of Cranio-Maxillofacial Surgery, 2009. **37**(3): p. 167-173.
24. Sugavaneswaran, M. and G. Arumaikkannu, *Analytical and experimental investigation on elastic modulus of reinforced additive manufactured structure*. Materials & Design (1980-2015), 2015. **66**: p. 29-36.
25. Li, Y., et al., *Cost, sustainability and surface roughness quality—A comprehensive analysis of products made with personal 3D printers*. CIRP Journal of Manufacturing Science and Technology, 2017. **16**: p. 1-11.
26. Stichel, T., et al., *A Round Robin study for selective laser sintering of polymers: Back tracing of the pore morphology to the process parameters*. Journal of Materials Processing Technology, 2018. **252**: p. 537-545.

27. Duan, B., et al., *Three-dimensional nanocomposite scaffolds fabricated via selective laser sintering for bone tissue engineering*. *Acta biomaterialia*, 2010. **6**(12): p. 4495-4505.
28. Yuan, S., et al., *3D soft auxetic lattice structures fabricated by selective laser sintering: TPU powder evaluation and process optimization*. *Materials & Design*, 2017. **120**: p. 317-327.
29. Bai, J., et al., *The effect of processing conditions on the mechanical properties of polyethylene produced by selective laser sintering*. *Polymer Testing*, 2016. **52**: p. 89-93.
30. Salmoria, G., et al., *Characterization of PA12/PBT specimens prepared by selective laser sintering*. *Optics & Laser Technology*, 2018. **98**: p. 92-96.
31. Kumar, S., *Selective laser sintering/melting*. 2014.
32. Schmid, M. and K. Wegener, *Additive manufacturing: polymers applicable for laser sintering (LS)*. *Procedia Engineering*, 2016. **149**: p. 457-464.
33. Kruth, J.-P., et al. *Part and material properties in selective laser melting of metals*. in *Proceedings of the 16th international symposium on electromachining*. 2010.
34. Carter, L.N., et al., *The influence of the laser scan strategy on grain structure and cracking behaviour in SLM powder-bed fabricated nickel superalloy*. *Journal of Alloys and Compounds*, 2014. **615**: p. 338-347.
35. Tan, K., et al., *Scaffold development using selective laser sintering of polyetheretherketone–hydroxyapatite biocomposite blends*. *Biomaterials*, 2003. **24**(18): p. 3115-3123.



36. Savalani, M., et al., *The effects and interactions of fabrication parameters on the properties of selective laser sintered hydroxyapatite polyamide composite biomaterials*. Rapid Prototyping Journal, 2012. **18**(1): p. 16-27.
37. Salmoria, G.V., et al., *Structure and mechanical properties of cellulose based scaffolds fabricated by selective laser sintering*. Polymer Testing, 2009. **28**(6): p. 648-652.
38. Almagrouk Mousa, A., *Experimental investigations of curling phenomenon in selective laser sintering process*. Rapid Prototyping Journal, 2016. **22**(2): p. 405-415.
39. Dorigato, A., M. D'Amato, and A. Pegoretti, *Thermo-mechanical properties of high density polyethylene–fumed silica nanocomposites: effect of filler surface area and treatment*. Journal of Polymer Research, 2012. **19**(6): p. 9889.
40. Yap, C., C. Chua, and Z. Dong, *An effective analytical model of selective laser melting*. Virtual and Physical Prototyping, 2016. **11**(1): p. 21-26.
41. Shirazi, S.F.S., et al., *A review on powder-based additive manufacturing for tissue engineering: selective laser sintering and inkjet 3D printing*. Science and Technology of Advanced Materials, 2015. **16**(3): p. 033502.
42. Chalancon, A. and D. Bourell. *Measured Energy Densities For Polyamide 12 And Comparison Of Values Calculated For Laser Sintering*. in *Proceedings of the Solid Freeform Fabrication Symposium, Austin, Texas, USA*. 2016.
43. Standard, A., *D882 2010 Standard Test Method for Tensile Properties of Thin Plastic Sheeting*. ASTM International, West Conshohocken, 2003.

44. Standard, A., *D638: Standard test method for tensile properties of plastics*. West Conshohocken (PA): ASTM International, 2010.
45. Kolan, K.C., et al., *Effect of material, process parameters, and simulated body fluids on mechanical properties of 13-93 bioactive glass porous constructs made by selective laser sintering*. *Journal of the mechanical behavior of biomedical materials*, 2012. **13**: p. 14-24.
46. Niebling, F., A. Otto, and M. Geiger. *Analyzing the DMLS-process by a macroscopic FE-model*. in *Proc. of 13th Solid Freeform Fabrication Symposium*. 2002.
47. Vasquez, G., et al., *A targeted material selection process for polymers in laser sintering*. *Additive Manufacturing*, 2014. **1**: p. 127-138.
48. Kruth, J.-P., et al., *Lasers and materials in selective laser sintering*. *Assembly Automation*, 2003. **23**(4): p. 357-371.
49. Tang, W., M.H. Santare, and S.G. Advani, *Melt processing and mechanical property characterization of multi-walled carbon nanotube/high density polyethylene (MWNT/HDPE) composite films*. *Carbon*, 2003. **41**(14): p. 2779-2785.
50. Souza, P., et al., *Mechanical properties of HDPE/textile fibers composites*. *Procedia Engineering*, 2011. **10**: p. 2040-2045.